Unterschrift Betreuer*in

DIPLOMARBEIT

A fingerprint approach for foehn events over Western Austria in the past and future

ausgeführt am Institut für Theoretische Physik der Technischen Universität Wien
in Zusammenarbeit mit dem Institut für Meteorologie und Klimatologie der Universität für Bodenkultur Wien

unter der Anleitung von
Herbert Formayer (BOKU Wien)
Florian Libisch (TU Wien)

durch

Philipp Maier BSc
Matrikelnummer 01614332

May 10, 2023

Unterschrift Student*in

Abstract

Foehn has a climatological impact on vegetation in Western Austria due to the drying effect caused by stronger windspeeds and rising temperatures. As there are regions, where foehn occurs on 10-20 % of the days, it is advisable to analyse possible changes in foehn behaviour in the wake of climate change to better estimate, which trees to cultivate on foehn-affected slopes.

To analyse foehn occurrence in the future and therefore independent from station data, gradient boosted tree models were used to link historic weather station data and synoptic patterns of reanalysis data over the Alpine area. A training data set for daily foehn occurrence was created from eleven years of selected semi-automatic weather station data by applying Objective Foehn Classification. By counting affected valley stations, foehn events were divided into local and widespread events. To allow an application on climate change projections, the selection of physically meaningful features was limited by the availability of variables in EURO-CORDEX models. With this approach, two XGBoost models per region were trained with accuracies of over 95 % for classifying between no foehn and foehn and over 84 % for deciding between localised and widespread foehn during the training period (2011-2021). These algorithms were then applied on ERA5 reanalysis data and on three models of the OEKS-15 ensemble of EURO-CORDEX climate scenarios to be able to analyse possible changes in foehn behaviour until 2100.

For every detected foehn day in the past and future, ground wind fields generated from interpolated stations were replaced with a wind field representing foehn in the affected regions. For that purpose, WRF simulations of selected, suitable foehn events which occurred during the training period were used as base fingerprints. The WRF wind fields were additionally scaled using a regression of the 500 hPa model and the fingerprint wind speed on the specific days and statistical noise. The replacements yielded wind climatologies with stronger winds on foehn-affected slopes and in valley elevations.

Zusammenfassung

Föhn hat durch stärkere Windgeschwindigkeiten und steigende Temperaturen klimatologische Auswirkungen auf den Austrocknungseffekt der Vegetation in Westösterreich. Mit einer jährlichen Häufigkeit von 10 - 20 % in einigen Regionen ist es notwendig, die Änderung der Föhnhäufigkeit und -intensität aufgrund des Klimawandels zu analysieren, um bessere Einschätzungen über die Baumarten bei der Kultivierung von föhnbetroffenen Hängen machen zu können.

Um Föhn in der Zukunft und damit unabhängig von Stationsdaten analysieren zu können, wurden Gradient Boosted Tree Models verwendet, um historische Stationsdaten mit synoptischen Wettermustern von Reanalysedaten in der Alpenregion mitenander zu verknüpfen. Ein Traningsdatenset mit täglichen Information über Föhnauftreten wurde aus elf Jahren an Daten von ausgewählten teilautomatischen Wetterstationen mittels Objective Foehn Classification generiert. Föhn kann durch das Zählen der betroffenen Talstationen als lokales oder großräumiges Ereignis klassifiziert werden. Um diese Methodik auch auf Klimaszenarien anwenden zu können, wurde die Auswahl der physikalisch relevanten Features durch deren Verfügbarkeit in EURO-CORDEX-Modellen limitiert. Mit dieser Methodik wurden zwei XGBoost Modelle pro Region trainiert, welche eine Genauig-keit von über 95 % bei der Klassifkation zwischen Föhn und kein Föhn und über 84 % bei der Klassifikation zwischen lokalisiertem und großflächigem Ereignis innerhalb des Traningszeitraums (2011-2021) erzielten. Diese Algorithmen wurden anschließend auf die ERA5-Reanalyse und auf drei Klimaszenarien des ÖKS-15 Ensembles der EURO-CORDEX-Modelle angewandt, um eine mögliche Änderung der Föhnhäufigkeit und -intensität bis 2100 analysieren zu können.

Für jeden detektierten Föhntag in der Vergangenheit und Zukunft wurden Bodenwindfelder, die durch flächig interpolierte Wetterstationen generiert wurden, mit einem für Föhn repräsentativen Windfeld ersetzt. Zu diesem Zweck wurden WRF-simulierte Bodenwindfelder von ausgewählten Föhnereignissen, die innerhalb der Traningsperiode auftraten, als Fingerprint verwendet. Zusätzlich wurden diese WRF-Windfelder mittels einer Regression der 500 hPa Model- und Fingerprintwindgeschwindigkeit und statistischem Rauschen skaliert. Diese ersetzten Windfelder lieferten Windklimatologien mit stärkeren Winden an föhnbetroffenen Hängen und auf Talböden.

Contents

1. Introduction

By the definition of the World Meteorological Organisation (WMO), foehn is a wind, which is warmed and dried by descent on the lee sides of mountains [1]. Driven by synoptic flows and cross-mountain pressure gradients, it replaces valley air masses, rapidly changing air temperatures, air pressures and humidity on a mesoscale level [2]. In fig. 1.1 a schematic of the foehn phenomenon is visible. Wind perpendicular to the mountain ridge descends dry-adiabatically from upper layers, conserving potential temperature θ along streamlines. The air mass gains speed during the descent into the valley. Amongst other effects such as endangering transportation, increasing risk of fire and improving air quality, foehn directly affects vegetation-growth due to its drying effect caused by higher wind speeds, increased temperatures and decreased humidity [2, 3, 4]. The strongest foehn events primarily occur in winter and last for several days but usually produce severe gusts within hours. These gusts are able to damage forests and constructions and the resulting turbulent flows are a serious hazard for aircraft [2].

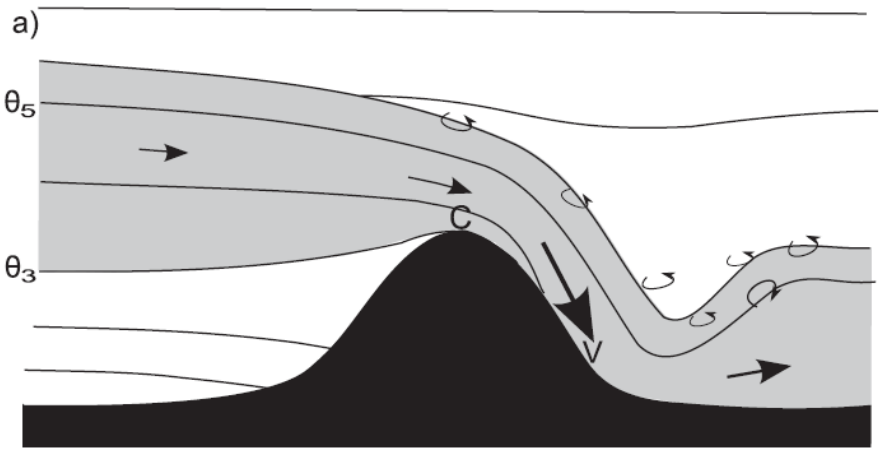

Figure 1.1.: *Schematic of the foehn mechanism. The foehn flow, which descends from the crest (C) to the valley (V) is coloured in dark-grey. Arrows show the average direction of the wind, where the arrow sizes indicate the wind speed. Curved arrows mark turbulent flows. Lines describe streamlines with conserved potential temperature θ. [5]*

With a climatological foehn occurrence of 10 - 20 % in certain regions of Western Austria, realistic input wind fields representing foehn to study vegetation are required [5]. In fig. 1.2 two daily mean wind speeds of the 3rd of March 2017 over Western Austria of already available products can be seen. While the upper wind field was provided by the Integrated Nowcasting through Comprehensive Analysis (INCA) project by the Central Institute for Meteorology and Geodynamics (ZAMG), the lower wind field was created by interpolating stations spatially by contributors of the same project, of which this thesis originated [6, 7, 8]. Both wind fields show a clear dependency on elevation and low wind speeds in valleys.

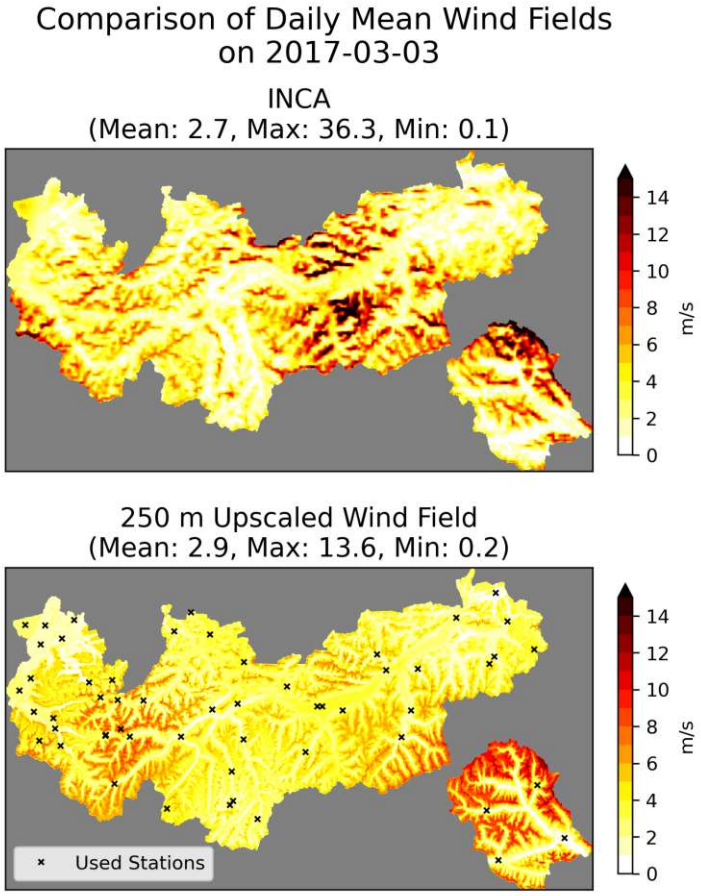

Figure 1.2.: *Comparison of daily mean wind speeds on the 3rd of March 2017 of two already available products for the project domain Western Austria. The colourbar describes wind speed values in* m/s. *Stations used to create the interpolated wind field in the bottom plot are marked with black crosses. Mean, maximum and minimum values are calculated over the whole area.*

A south foehn breakthrough occurred on the same day. In fig. 1.3 a simulated, physically consistent mean wind field of the same day is displayed [9]. Higher windspeeds in valleys are observed compared to the other wind fields and no clear dependency on elevation is visible. The washed out patterns indicate, that air layers are mixed. By comparing foehn patterns like the example below with the mean wind fields above, other experts decided, that INCA and our station interpolated wind field fail in interpolating station wind into ground wind fields in a realistic way during foehn days due to large distances between stations [8]. As both wind fields were interpolated from stations, they match the observations at measurement sites. But the available data sets over Western Austria are not able to produce realistic foehn wind patterns with high resolution outside of station locations and fail to describe the mixing of air layers [8].

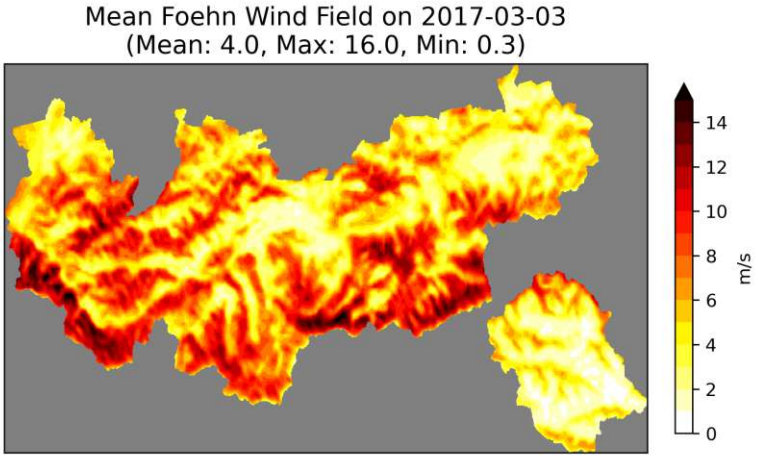

Figure 1.3.: *WRF simulated mean wind field on the 3rd of March 2017. The colourbar describes wind speed values in* m/s. *Mean, maximum and minimum values are calculated over the whole area.*

Wind climatologies and therefore wind fields representing foehn events have to be generated in locations with absent station data for providing a meteorological base to study the impact of foehn on vegetation. So far, no method is available to accomplish the task of considering foehn directly in wind fields. Foehn is only indirectly present through station data, yielding no information about spatial distribution of air flows. For the purpose of producing a method which considers foehn directly, the following research questions have to be answered:

- Can a detection algorithm be established to detect foehn events in reanalysis data as well as in climate projections, thereby being independent of station data?
- Does foehn show similar patterns over the Alps and can the patterns be separated by the algorithm into different intensities and affected regions?
- Are climate projections able to produce similar weather patterns, allowing foehn to occur?
- How would a fingerprint approach for distinguishing foehn in different regions and for different intensities be simulated and scaled to generate diverse wind fields with fine resolution?

To answer those questions, chapter 2 introduces the theoretical background of foehn as well as explains the basics of weather and climate models and the used machine learning approach. Chapter 3 lists the used data, describes how a training data set was created and how the machine learning algorithm was applied to extract days with foehn occurrence of different strength. It also shows, how physically consistent, simulated foehn wind fields are scaled to produce foehn climatologies. Chapter 4 displays results and discusses, if our approach was able to answer the research questions. Finally, chapter 5 concludes the thesis and gives an outlook, how the methodology can be improved in the future.

2. Theoretical Background

2.1. The Effect of Topography on Wind Systems

Terrain-forced winds like foehn occur when synoptic wind is modified by underlying terrain [3]. In contrary, diurnal winds are caused by temperature differences on mountain slopes [3]. When approaching a barrier, the behaviour of an air mass is strongly dependent on the air's stability, wind speed and the underlying terrain itself [10]. The more stable, the more resilient the air is to being lifted. Strong pressure gradients are required for stable air to be lifted over a barrier [10]. Mountain barriers are able to block incoming air flows, which most often occurs when stable air masses in winter form a local high pressure centre, which counteracts synoptic pressure gradients [3]. The air mass then builds cold pools of dead air on the windward side of the mountain.

Especially on isolated peaks, the air is more likely to flow around, split or flow through gaps, yielding strong wind zones on the edges of the mountain [3]. Forced channelling of wind aloft often occurs during strong winds, especially in mountain passes like the Brenner pass, the south end of the Wipp Valley. The wind is then accelerated due to the Bernoulli-effect caused by smaller diameters of the gaps, channels and passes. Those terrain induced effects accelerate air masses [3].

2.2. The Foehn Phenomenon

Foehn research has a long history, started by Julius von Hann in 1885 [11]. The origin of foehn air masses was long debated with several theories, where one proposed explanation was, that foehn air masses originate in the Caribbean and Sahara due to its dry properties [12]. Hann was the first to state, that foehn has thermodynamical reasons, where air masses are moist in upper layers and dried by descent [12].The theory was underpinned by the recording of north foehn in the alpine area and the fact, that foehn was observed on several mountain ranges, counteracting the idea of the origin of air masses in dry regions. Hann and Ficker subsequently became known as the developers of the Thermodynamic Foehn Theory, which is still present in textbooks today in modified form [11, 12, 13].

2.2.1. Thermodynamic Foehn Theory

In the Thermodynamic Foehn Theory, synoptic pressure gradients force humid air towards a barrier on the luv side of the mountain. Because of the forced lifting, the air cools dry-adiabatically with a lapse rate of 9.8 °C/km until it reaches saturation. From the point of saturation it continues to cool with a saturated adiabatic lapse rate of approximately 5-6 °C/km [3]. Heat is gained by wet-adiabatic lifting until the air reaches the crest. Latent heat is released in the luv, clouds form and precipitation occurs [3]. The wind then descends on the barrier's leeward side. The adiabatic compression of the air causes the wind to warm up and dry out with the dry-adiabatic lapse rate of 9.8 °C/km [3]. Because molecules have higher kinetic energy, warmer air is able to store more water than colder air [14]. The amount of water bound in the air is constant. In consequence, relative humidity decreases. The descending warm air penetrates and replaces cold valley air masses, having an effect on several meteorological variables. Temperature increases, humidity decreases and potential temperature (see section 2.3.3) is higher compared to the air on the luv side [15]. Visibility and air quality improves. A so called foehn window is present, which can prevent nocturnal temperature inversions from forming [15].

While Thermodynamic Foehn Theory is an elegant way of displaying thermodynamical weather systems, the process described above marks an extreme situation of foehn. Foehn was also observed, when upwind air in the luv was partially or completely blocked, forming dead air pools without precipitation [15]. Strong inversions are therefore able to separate cold air pools from the upper, warmer air. Precipitation is no proof for the gain of latent heat, because it can occur from clouds not part of the foehn flow [15]. An illustrative example with separated air masses is the so called century foehn in November 1982 in the Wipp Valley, which was the strongest foehn ever recorded up to that point in time [15, 16].

Foehn therefore also occurs without wet-adiabatic heat gain and latent heat release, making precipitation a feature of foehn and not a requirement [16]. Precipitation further has no major influence on the temperature increase in the lee [16]. Hann predicted the subordinate role of latent heat release as well, which resulted in a correction of his own theory [11]. In fig. 2.1 the original theory of foehn formation is compared to the corrected one, where the foehn air masses originate from upper layers. Separation of air masses and stability in the figure is shown through the potential temperature relations, which is described in section 2.3.3.

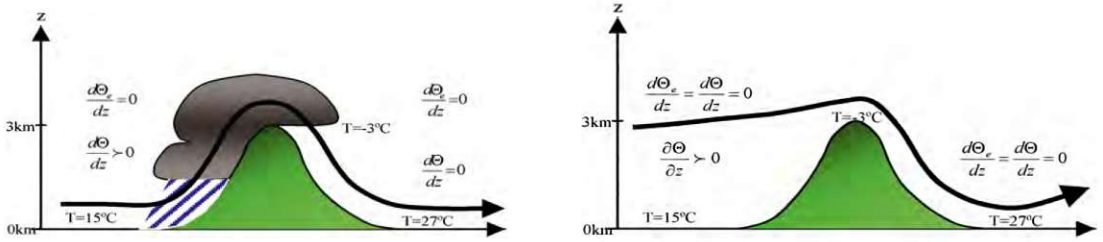

(a) *Original foehn theory* (b) *Corrected foehn theory*

Figure 2.1.: *Comparison of traditional and corrected foehn theory. In the original theory, the latent heat release during precipitation was described to be a requirement for foehn to build as shown in (a). The corrected, today still valid theory is shown in (b). It states that foehn winds (can) come from upper layers and a separated pool of dead air is present in the valley in the luv. This dead air pool may or may not form precipitation. Stability information is given by the vertical gradient of the potential temperature* $\frac{\partial\theta}{\partial z}$*.[17]*

Fig. 2.2 shows a typical south foehn condition over Austria. In valleys on the Alps' northern side significantly higher temperatures are visible across all regions, which is one of the indicators for foehn air masses in the valley [6]. Warm air flows are also visible in the Alps' outlets.

Figure 2.2.: *Typical south foehn condition in Austria, obtained with INCA on the 21st of October 2020 at 1 a.m [6]. The colourbar indicates values in* °C*. In the valleys on the Alps' northern side, values above* 20 °C *can be observed.*

2.2.2. Theories on the Descending of Foehn

Why foehn is able to penetrate valley air pools is a highly studied subject of the foehn's flow dynamic. The vertical structure of air masses in valleys is crucial while moist processes play no significant role in the descent of foehn [18]. Other effects influencing the descent are heating by convection and solar radiation, static and dynamic displacement and erosion of the top by mixing and entrainment [19]. These effects vary from valley to valley. Therefore, no theory is applicable in all situations [15]. For example, foehn in the Inn valley strongly correlates with the sun cycle and therefore has more thermodynamic influences, while foehn in the Wipp Valley relies more on dynamics [19].

Several theories on the descending of foehn were proposed, which are summarised in [13, 15, 17] and recited below.

- **Vertical Aspiration Theory (Streiff-Becker, 1933):** Turbulent erosion of warm air scours away cold air pools in the valley. The potentially warmer air from above then sinks gradually into the valley, replacing the cold air.
- **Horizontal Aspiration Theory (Ficker, 1912):** An approaching Atlantic low drags the cold air masses away through the valley's outlets. The warmer air aloft functions as replacement flow, which is why the theory is also called Passive Replacement Theory.
- **Lee Wave Theory (Lyra, 1940 and Queney, 1948):** Lee or gravity waves describe a phenomenon, where stable air flows over a barrier and begins to fluctuate around the equilibrium level of the cooling air in its new leeward environment [3, 10]. The air overshoots during cooling, causing the air parcel to go back up the atmosphere, where it overshoots again [10]. Perpendicular or even concave massifs of high mountains and decreasing vertical stability favour the formation of lee waves [10]. When winds become stronger and still show an increase with height, deeper waves tend to form, which then propagate further downward where strong rotors form [10]. These high amplitude lee waves force foehn to penetrate the valley by depressing the surface near the edge of the cold valley air. Under certain, sharply defined stability, flow and orographic conditions, a large-scale instability can cause the entire mountain wave to flow down the lee side with high wind speeds [10].
- **Solonoid Theory (Frey, 1944):** Rotational accelerators called solonoids build because of different orientations of pressure and temperature gradients on the lee side of the mountain. They enhance the acceleration of air masses imposed by the pressure gradient, giving the air enough kinetic energy to penetrate cold air pools.
- **Waterfall Theory (Rossmann, 1950):** Precipitation in the luv causes a cloud wall on the crest, the so called foehn wall to build. These clouds are colder and denser than its surrounding air, causing it to accelerate downward. With sufficient kinetic energy, it penetrates cold air pools. This theory is only applicable in classical thermodynamic foehn events.

- **Hydraulic Theory (Schweitzer, 1953):** The Hydraulic Theory can be used to describe gap flows, which satisfy foehn criteria because the flow is compressed and warmed by gaps within the barrier. Hydraulic Theory is also used for shallow foehn, where no dominant flow perpendicular to the mountain ridge occurs in higher altitudes [18, 20, 21]. During shallow foehn, upper and lower flow patterns are completely distinct and the foehn is considered as compensation flow between air masses on both sides of the mountain, where the valleys have different temperatures [16]. A famous foehn location with properties of a gap is the Brenner Pass, which reaches into the Wipp Valley [20]. Using shallow water theory, the foehn flow is modelled using the Froude number

$$\mathrm{Fr} = \frac{u}{gL}\,, \tag{2.1}$$

where u is the local flow velocity, g is the gravitational acceleration and L is the characteristic length of the problem, in this case the length of the slope. Fr is an indicator for the state of the fluid. For $\mathrm{Fr} < 1$ the velocity is less than the speed of gravitational waves and is subcritical. For $\mathrm{Fr} > 1$ the flow velocity exceeds the wave speed and is not able to respond to changes in surrounding parameters like temperature, air movement and pressure [20]. In consequence, the high speed fluid can only propagate downstream and breaks into regions with significantly lower flow speeds, causing an abrupt speed rise of the slower moving fluid and turbulence. This transition with $\mathrm{Fr} \approx 1$ is called a hydraulic jump and is normally observed in rivers [20]. The flow points in the direction with $\mathrm{Fr} < 1$, transitioning back into a subcritical state [20]. Hydraulic jumps are associated with rotors and strong turbulence by transforming kinetic energy of the flow into turbulent motion [10]. A prominent location for hydraulic jumps is in the Wipp Valley between Ellbögen and Innsbruck [20].

2.3. Classification of Foehn

A fall wind is classified as foehn if the wind has a pronounced direction and speed perpendicular to the mountain ridge and if the potential temperature between ridge and valley are similar indicating the same air mass. This method is called Objective Foehn Classification (OFC) [18, 19]. For using OFC, at least two reference points, one on the mountain crest and one in the valley are required. The foehn is forced by synoptic cross-alpine surface pressure gradients [15]. In the following subsections, variables possibly implying foehn are described briefly. Afterwards, the history of foehn classification is stated.

2.3.1. Cross-Barrier Mean Sea Level Pressure

Air masses with different temperature on different sides of barriers cause large pressure gradients. These gradients produce strong ground winds [18]. To remove the effects of underlying orography the Mean Sea Level Pressure (MSLP), which is the surface pressure normalised to the mean sea level, is used in weather maps [14]. Pressure gradients are an indicator for the strength of the foehn event, because pressure and wind speed are directly connected through the flow dynamics [19]. The pressure gradient is also partly a consequence of foehn itself, because it brings warmer and less dense air into valleys [18]. In fig. 2.3 a characteristic MSLP field over the Alps, which is often called foehn nose or foehn knee, is visible. Strong cross-barrier gradients are visible. In Eastern Austria, where the topography is flatter and pose a weaker barrier, the high pressure field mitigates towards the north, yielding the foehn nose. Still, without information about the stability and layering of the atmosphere, the MSLP is not enough to forecast foehn because of the lack of wind speeds aloft.

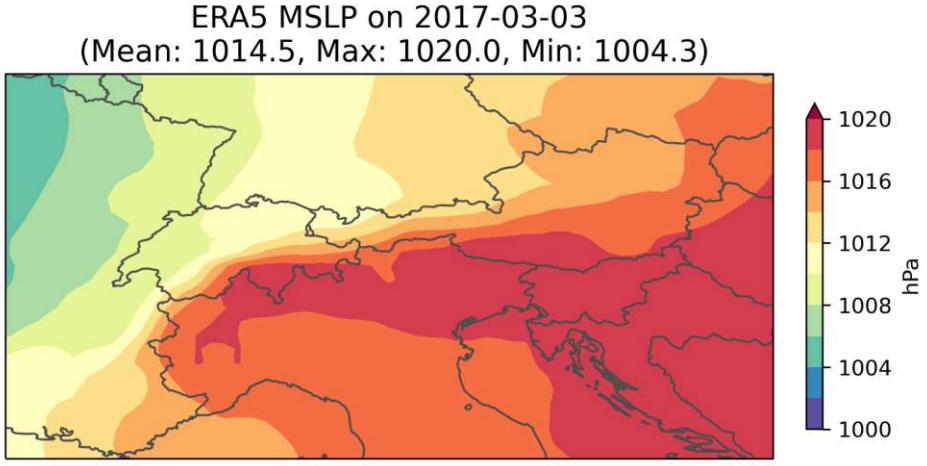

Figure 2.3.: *Typical foehn MSLP field on the 3rd of March 2017. The colourbar describes pressure values in* hPa. *Mean, maximum and minimum values are calculated over the whole area. A high pressure gradient is visible over the main ridge of the Alps. [22]*

2.3.2. Wind Direction and Wind Speed on the Crest and in Valleys

Foehn is characterised by a rapid change towards high wind speeds and a constant wind direction perpendicular to the crest [15]. Likewise, the breakdown of foehn is determined by deviating wind directions. The intensity of foehn correlates with the ridge wind speed [2]. Observing wind at a mountain station therefore is suitable for getting information about the foehn strength. Foehn winds are generally stronger in valleys perpendicular to the mountain ridge due to less obstructions and flow channelling [15]. Wind speeds can be higher on the ground compared to aloft as well as shifted in direction due to forced channelling along the valley axis [15]. Along with the pressure gradient, crest-level flow and pressure gradient have the main impact on downslope winds [2].

In spatially coarse numeric weather prediction models (NWPs), the 700 hPa level, which is in approximately 3000 m in altitude, marks an ideal height for observing wind at the Alps' crest as the models' main ridge have an elevation of approximately 2300 m. With this height difference, air flows across and above crests can be simulated similar to reality [23]. When observing higher levels like 500 hPa, which is available in many climate scenario products, winds during foehn events tend to be stronger and shifted towards directions away from the axis perpendicular to the ridge.

2.3.3. Potential Temperature

The potential temperature is a concept to describe the potential and thermal energy of a dry air parcel. It is used to compare the temperature of air masses in different heights and pressure levels. The first law of thermodynamics describes the relation of thermal energy U, work W and heat Q

$$\mathrm{d}U = \delta Q + \mathrm{d}W\,. \tag{2.2}$$

For an adiabatic process, no heat is exchanged ($\delta Q = 0$) and the first law reduces to

$$\mathrm{d}U = \mathrm{d}W\,. \tag{2.3}$$

By Legendre-transforming the equation above, the adiabatic equation for an ideal gas with constant volume V, Temperature T and specific heat capacity under constant pressure for dry air $c_p = 1005\,\mathrm{J\,kg^{-1}\,K^{-1}}$, is described with the enthalpy H [14]:

$$\mathrm{d}H = c_p \mathrm{d}T = V\mathrm{d}p\,. \tag{2.4}$$

By inserting the ideal gas equation for air

$$pV = R_{\mathrm{air}}T\,, \tag{2.5}$$

where $R_{\mathrm{air}} = 287\,\mathrm{J\,kg^{-1}\,K^{-1}}$ is the gas constant for air, equation 2.4 yields [14]:

$$\frac{\mathrm{d}T}{T} = \frac{R_{\mathrm{air}}}{c_p}\frac{\mathrm{d}p}{p}\,. \tag{2.6}$$

Integration to a certain height z by using the standard pressure at sea level $p_0 = 1013.25\,\mathrm{hPa}$ yields the definition of the potential temperature in Kelvin [14]:

$$\theta(z) = T(z)\left(\frac{p_0}{p_z}\right)^{\frac{R_{\mathrm{air}}}{c_p}}\,. \tag{2.7}$$

The potential temperature $\theta(z)$ therefore describes the temperature of a dry air parcel at height z with $T(z)$ and $p(z)$, when it is dry-adiabatically reduced to p_0.

Potential temperature is one of the quantities, which is conserved along streamlines when foehn is descending into valleys without precipitation occurring in the lee. That makes potential temperature a possible tracer for foehn, where small differences indicate same air masses. While temperature measurements and simulations have to be accurate for good tracing, pressure inaccuracies have less impact [18]. The usage of potential temperature as tracer is limited by wet-adiabatic effects and temperature advection during the travel time of the air. Solar radiation and turbulent mixing can also be other limiting factors [18].

Ideally, vertical air masses are dry-adiabatically mixed during foehn events. The potential temperature difference between the crest and the valley during foehn is therefore close to zero. While positive values of the difference between ridge and valley indicate no or only weak descent, neutral or slightly negative values indicate strong descents [2]. In fig. 2.4 vertical profiles of potential temperatures during cold seasons are visible. It displays different foehn related weather situations, showing the same potential temperature at the crest and valley during foehn events with breakthrough. A breakthrough is indicated by matching potential temperatures in valley and crest elevations.

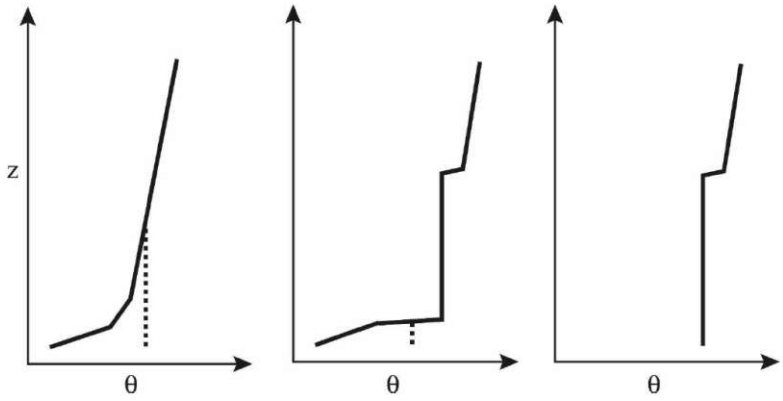

Figure 2.4.: *Cold season vertical profiles of potential temperature θ with height z during no foehn (left), a foehn case without breakthrough (middle) and with breakthrough (right). Solid lines describe morning hours, dashed lines afternoon hours. [2]*

On the windward side, potential temperature is cooler compared to the lee side. An increasing potential temperature on the windward side implies thermodynamic foehn conditions [15]. The potential temperature difference between blocked air and the actual foehn flow in the luv hereby is a parameter for distinguishing between foehn with and without precipitation [15]. For foehn involving precipitation the difference would be zero ideally.

North foehn events have less pronounced warming characteristics because the flow moves in the direction of the positive north-south temperature gradient [15]. North foehn occurrence is dependent on where low pressure centres pass the Alps. The closer to the Alps, the higher the chance of north foehn will be because of the more frequent occurrence of north wind components [24]. Therefore, north foehn can occur as post-frontal phenomenon of any low pressure centre, which yields north components in wind speed [23].

Potential temperature is also a measure for the atmosphere's stability. For $\frac{\partial\theta}{\partial z} < 0$, the layers are unstable. An air parcel will continue to rise in this condition. For $\frac{\partial\theta}{\partial z} > 0$ the air is stable, an air parcel will sink down again under this condition. $\frac{\partial\theta}{\partial z} = 0$ marks a neutral atmosphere [14].

2.3.4. Humidity

Any humidity parameter could suffice to detect a rapid change in moisture, when dry foehn air descends onto a specific valley station. In this thesis, the relative humidity

$$\mathrm{rh} = \frac{p_w}{p_{w,sat}} = \frac{\rho_w}{\rho_{w,sat}} \tag{2.8}$$

where p_w (ρ_w) is the actual water pressure (density) and $p_{w,sat}$ ($\rho_{w,sat}$) is the saturated water pressure (density), was the parameter of choice [14]. Water content stays the same during a dry descent of foehn. Warm air is able to store more water because of the higher kinetic energy collisions of the air's molecules, allowing the water to stay in a gaseous state more often [14]. As a consequence, relative humidity decreases on the lee of the mountains to at least 60 % in typical cases [15].

An absolute parameter of humidity, often available in climate models is the specific humidity q, which is the mass of water vapour in a unit mass of moist air, usually stated in g/kg. An approximation of how to convert specific humidity q of an air parcel in g/kg with the pressure p in Pa and Temperature T in K in is given by

$$\mathrm{rh} = 0.263pq[e^{\frac{17.67(T-T_0)}{T-29.65}}]^{-1} \tag{2.9}$$

where $T_0 = 273.15\,\mathrm{K}$ is the reference temperature [25]. Absolute humidity parameters are another possible choice for tracing foehn, as these variables are also conserved along streamlines.

2.3.5. History of Classification Methods

The traditional way of classifying foehn using a single valley station was a three-criteria definition. It requires wind speed and direction coming from the mountain, temperature increase and humidity decrease, solely at the valley station [19]. The thresholds of these criteria are highly subjective and dependent on the user. In summer, foehn air masses may be colder compared to the pool in the valley, violating the temperature and relative humidity criteria [19]. These criteria are therefore only valid, when the air masses between crest and valley are dry-stable. The three-criteria also makes it difficult to distinguish foehn occurrences from strong thermally driven winds or outflows.

Synoptic surface pressure patterns are one of the most useful tools for classifying foehn [15]. To judge, which valleys are affected, a forecaster's rule states without proof yet, that foehn typically descends within 200 m of the mountain ridges over which it streamed in [15]. Adding mesoscale surface pressure patterns and upper air flows to the three-criteria definition improves classification, but it makes it still difficult to decide if foehn occurs at given locations [18].

Over the course of the Mesoscale Alpine Program in 1999, an objective, physically based foehn classification using station data of one mountain station and one valley station was presented. It uses wind direction and speed at the crest and potential temperature difference between those two references for classifying. This is the classification scheme still valid today, the aforementioned OFC [18]. Since then potential temperature is a variable commonly used for automatic foehn detection [2, 5, 19, 26]. Statistical mixture models, which use the same variables to give a likelihood of foehn occurrence rather than absolute thresholds for classifying, further improve OFC [5].

Most foehn classification tools are using data from stations and not from NWPs [5, 26]. With increasing spatial resolution, there is hope that models will provide sufficiently accurate weather patterns that result in foehn. Progress was made using probabilistic and machine learning approaches. For example, the authors in [2] use synoptic pressure and potential temperature differences in a coarse NWP to apply a probabilistic algorithm for foehn forecasting. Machine learning with station data as training data is used to connect NWPs with foehn events. The trained machine learning algorithms are able to generalise, extending foehn predictions into future and past scenarios, where no station data is available [27, 28, 29]. This thesis takes a similar machine learning approach.

2.4. XGBoost

XGBoost is a scalable tree boosting system, which uses fewer resources than existing systems [30]. It is used in a wide variety of problems including store sales predictions, malware classification and high energy physics classification due to its scalability made possible by system and algorithmic optimisations [30]. These optimisations are sparsity-aware algorithm design for parallel tree learning, a theoretically justified weighted quantile sketch for efficient proposal calculation and an effective cache-aware block structure for out-of-core tree learning, all combined in an end-to-end tree boosting system [30].

The basis of this method builds the ensemble learning method called random forest approach. Random forests are a set of individual decision trees, which classify or apply a regression independently from each other [31]. Each node of a decision tree, poses a question regarding one of the features it obtains. Features are a set of variables describing each data point. The resulting decision is then passed to a child node, which does the same procedure with a different question for a different feature [32]. Decisions either could be made by applying hard thresholds or simple regressions. This process is repeated until a so called leaf node is reached and the data is categorised [32]. Each tree gets a random subset of features, which can be e.g. meteorological input variables. The trees are trained on different random sets of the training data to reduce correlation, using the same training data pair multiple times as replacement, which is called bootstrapping [31]. When shown new features, each decision tree decides on its own how to classify. The final prediction is the classification with the most aggregated votes [31]. An example of this procedure using regression is visible in fig. 2.5. One drawback of the random forest approach is, that it is less interpretable than a single decision tree. However, the averaged feature importance can be extracted out of random forest approaches, yielding the features with the highest weights [31].

A drawback of training individual decision trees not influencing each other is, that they are not able to learn from each other. Boosted tree models use an ensemble method called boosting, where new trees are formed by considering the errors of trees from previous training rounds [32]. New trees are therefore created sequentially, in an iterative way, and not independent of each other, transforming weak decision trees into strong learners [32]. Parallelizing the training is therefore difficult. As a result, training time is usually higher [30]. Boosted trees are a useful tool for classifying non linear data [30].

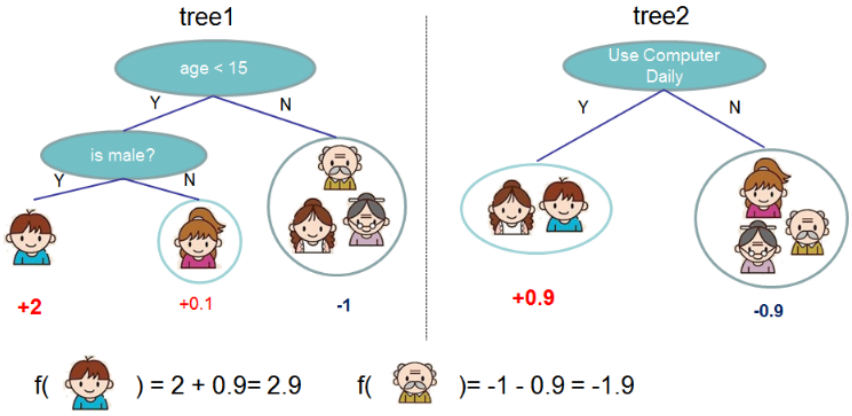

Figure 2.5.: *Example of the random forest approach. Each node gets a different feature from which to classify. The result then is the aggregation of all individual trees, yielding either a certain regression value like in the figure or a class affiliation. [30]*

XGBoost is one of these boosted tree approaches. The formal goal of a supervised machine learning approach like XGBoost is to make predictions $\hat{y}_i$ using a number of m features $\mathbf{x}_i \in \mathbb{R}^m$ from n events and their corresponding true labels y_i. In case of a regression problem, labels mark a regression value: $y_i \in \mathbb{R}$. In case of a classification, labels are class affiliations: $y_i \in \{0, 1\}$. To validate a prediction, convex loss functions l are used, which should be minimised along the training of the algorithm. Typical loss functions for classification can be the $\mathcal{L}_2$ norm

$$l(\hat{y}_i, y_i) = (\hat{y}_i - y_i)^2 \,, \tag{2.10}$$

or the logistic loss

$$l(\hat{y}_i, p) = -(\hat{y}_i \log(p) + (1 - \hat{y}_i) \log(1 - p)) \,, \tag{2.11}$$

where $p = \Pr(y = 1)$ is the probability for a label y to be attributed to the positive class [33].

A properly minimised loss function typically results in high accuracy acc in classification problems

$$\text{acc} = \frac{\text{TP} + \text{TN}}{\text{TP} + \text{TN} + \text{FA} + \text{ME}}\,, \tag{2.12}$$

where TP are the true positive, TN the true negative, FA the false alarm and ME the missed event predictions.

The approach of the XGBoost algorithm to perform this task is

$$\hat{y}_i = \phi(\mathbf{x}_i) = \sum_{k=1}^{K} f_k(\mathbf{x}_i)\,, \tag{2.13}$$

where $f_k \in \mathcal{F} = \{f(\mathbf{x}) = \omega_{q(x)}\}$ describes the space of classification (or regression) trees, f_k being one of K additive corresponding functions predicting the output of an independent tree structure q with leaf weights ω [30]. XGBoost uses a regularised objective to its regression or classification. In the XGboost algorithm, the regularised objective reads as

$$\mathcal{L}(\phi) = \sum_i l(\hat{y}_i, y_i) + \sum_k \Omega(f_k)\,, \tag{2.14}$$

where

$$\Omega(f) = \gamma T + \frac{1}{2}\lambda + \|\omega\|^2\,, \tag{2.15}$$

is a term which penalises model complexity and prevents overfitting to the training data [30]. T is the number of leaves in a decision tree with γ being its weighting to the loss function. The more leaves, the more complex a decision tree is. λ is the regularisation parameter, and ω describes the vector of leaf weightings. The model will therefore tend to train simple and predictive functions [30]. To iteratively train the model, this function is modified for iteration step t to

$$\mathcal{L}^{(t)} = \sum_{i=1}^{n} l(y_i, \hat{y}_i^{(t-1)} + f_t(\mathbf{x}_i)) + \Omega(f_t)\,, \tag{2.16}$$

and afterwards approximated by second-order gradient building, hence the name gradient boosting [30]. For a fixed structure $q(\mathbf{x})$, this yields the optimal weight on leaf j using by summing over its instance set $I_j = \{i|q(\mathbf{x}_i) = j\}$:

$$\omega_j^* = -\frac{\sum_{i \in I_j} g_i}{\sum_{i \in I_j} h_i + \lambda}\,, \tag{2.17}$$

where g_i and h_i are the first and second order gradient on the loss function. This yields the optimal value of the regularisation objective

$$\tilde{\mathcal{L}}(q) = -\frac{1}{2}\sum_{j=1}^{T}\frac{(\sum_{i \in I_j} g_i)^2}{\sum_{i \in I_j} h_i + \lambda} + \gamma T\,, \tag{2.18}$$

which can be interpreted as a scoring function to measure the quality of a tree structure q [30].

2.5. Numerical Weather Predictions and Climate Models

General Circulation Models (GCMs) are dynamic, three dimensional models, which are the most complex weather and climate models to this day. To study local variations of the climate, the Earth's atmosphere is divided into grid boxes. Most recent GCMs use a horizontal grid sized about 100 km and between 30 and 40 vertical atmospheric layers [34]. GCMs use a wide range of equations including the Navier-Stokes Equations for the air's circulation, coupling of radiative and non-radiative energy, interaction between the biosphere, cryosphere, hydrosphere and atmosphere and even chemical processes and aerosol formation [34]. An additional, coupled GCM is used for the ocean's circulation [34]. Fig. 2.6 shows a schematic of how the Earth is divided into grid cells and how the aforementioned physical interactions are part of GCMs. They produce output in form meteorological variables such as temperature in different layers of the atmosphere and ocean, wind speed and wind direction, precipitation and snow cover. Fig. 2.7 shows how the complexity of GCMs has evolved over the past decades [35]. Since the mid-1970s, new physical effects have been incorporated into the models, ranging from clouds, oceanic circulation, volcanic activity and aerosols to interactive vegetation [35]. Because some of these equations are non-linear differential equations, the models have to be solved numerically [34]. To prevent possible instabilities, time steps have to be sufficiently low, ranging from ten to 30 minutes [34]. GCMs are therefore computationally expensive to calculate.

To run GCMs, input data on the absorption of radiation is required. This includes changes in the sun's radiation output as well as concentration of green house gases and aerosols and is called radiative forcing [36]. Using different assumptions and estimations about anthropogenic green house gas emissions enables GCMs to act as climate models with different projections. In this thesis, climate scenarios with Representative Concentration Pathways (RCPs) as a measure for radiative forcing were used. RCPs are used to describe additional radiative forcing caused by anthropogenic emissions till the year 2100 compared to the pre-industrial level [37]. The RCPs range from 2.6 to 8.5 W/m^2 [37]. For example, RCP 4.5 represents 4.5 W/m^2 radiative forcing in 2100 compared to the pre-industrial level. Different GCMs forced with identical emission scenarios form an ensemble for different RCPs. To get a grasp of model uncertainty and performance, a single model is run with different experiment settings where one boundary condition or feedback strength is varied and the simulation is done again [34]. Which experiments to run is defined by the guidelines of the Coupled Model Intercomparison Projects (CMIP) [38]. Models with requirements from the fifth CMIP assessment report were used in this thesis.

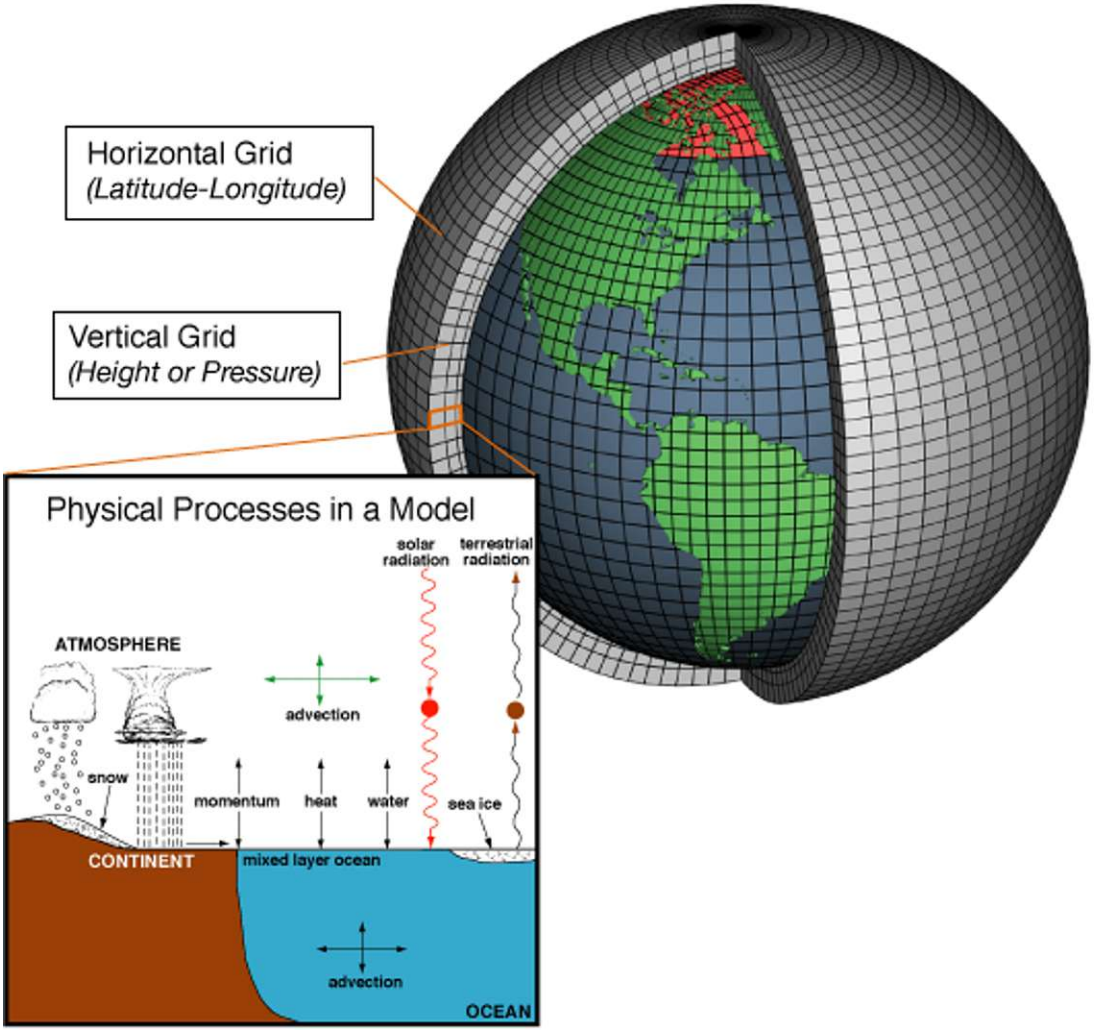

Figure 2.6.: *Schematic of a GCM. The Earth's atmosphere and ocean are divided into horizontal latitude-longitude grid cells. The atmosphere's vertical layers are gridded into height or pressure levels. GCMs include a number of physical processes including ocean-land-atmosphere interaction, heat and energy transfer and radiation budgets. Which of these processes are considered is visible in the boxed image, where the arrows indicated possible interactions and exchanges. [39]*

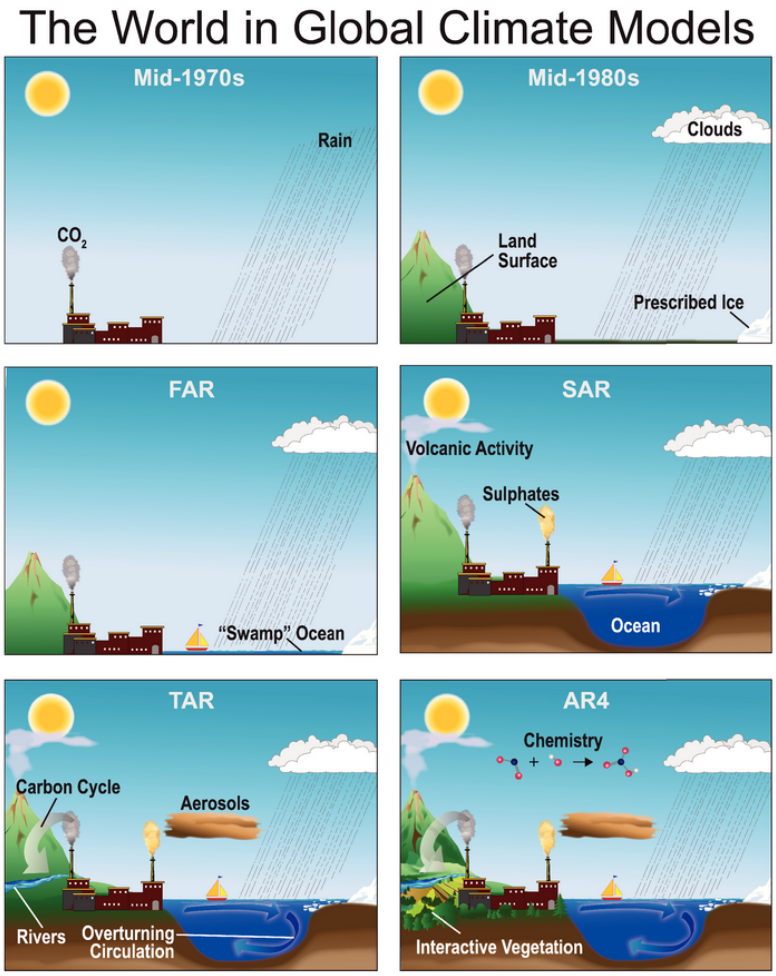

Figure 2.7.: *Development of GCM complexity. Different physical effects were incorporated since the mid-1970s, visible by black and white texts within the respective images. The abbreviations in the pictures describe different IPCC assessment reports, with FAR being from 1990, SAR from 1996, TAR from 2001 and AR4 from 2007. [35]*

The 100 km horizontal mesh grid is not enough for presenting local patterns. Therefore, one grid cell only describes the average characteristic of the covered area. Parametrization has to be used for processes like cloud formation, which occur within smaller horizontal distances than a 100 km grid cell [34]. Increasing the resolution would result in a multiple of required computation power as the underlying equations have to be applied to each grid cell. For the purpose of displaying smaller scale processes, statistical downscaling can be applied, where historical observational data is used to calculate a relationship between the local and global climate [40]. Dynamical downscaling using Regional Climate Models (RCMs) can be used as an alternative to statistical downscaling. RCMs are GCMs as well, but for specific regions using parameters from a global GCM as lateral boundary conditions. The nested RCM are therefore heavily dependent on the global GCM [34]. The same RCM will produce different outputs when forced with a different global GCM. Typically RCMs have no coupled ocean GCM. Values from the global ocean GCM are used for regions near oceans if they are required [34]. RCMs provide finer grids in the range of tens of kilometres or even lower. Due to its dynamical approach, it can provide sub-daily temporal resolution, which cannot be reached with statistical downscaling [41]. They improve representation of topography, land-sea contrast and soil characteristics [41].

Projects which use a GCM and force it to coincide with existing observations during running the experiment are called reanalysis. High quality observational data is required for running a reanalysis [22].

3. Material and Methods

3.1. Data Sources

- **ERA5**: The fifth generation of the European Centre of Medium-Range Weather Forecast's (ECMWF) reanalysis model of the atmosphere is called ECMWF Reanalysis 5th Generation (ERA5) [42, 43]. This global GCM has several variables available on surface and pressure levels, an hourly time scale and a horizontal mesh size of 0.25°, which translates to roughly 30 km in the European latitudes. The data was generated by assimilating climate models to existing observations [22]. Starting from 1951, it includes parameters of the atmosphere, land surface, ocean, sea ice and carbon cycle. For the feature matrix of the machine learning algorithm, temperature and specific humidity converted to relative humidity at 850 hPa, mean sea level pressure and wind components and geopotential at 500 hPa were used.
- **EURO-CORDEX**: EURO-CORDEX models are high-resolution climate change GCM ensembles, down-scaled to 12.5 km horizontal grid size [44]. Different RCPs are implemented, from RCP 2.6, roughly agreeing to the Paris agreement, RCP 4.5, where some climate protection measures are undertaken and RCP 8.5, which is often described as the business as usual scenario [37]. The models were created by downscaling global GCMs using different RCMs [44]. The OEKS-15 ensemble represents a selection of EURO-CORDEX models suitable for Austria, covering a variety of possible scenarios [45]. The same variables as in ERA5 of three of these models were selected and patch-regridded on the ERA5 grid to analyse change in foehn behaviour over different climate scenarios. The model names are descriptively stated in the form of GCM_RCP_ensemble_institute-RCM and were:

  - MPI-M-MPI-ESM-LR_rcp45_r1i1p1_CLMcom-CCLM4-8-17 (short: MPI rcp45)
  - MPI-M-MPI-ESM-LR_rcp85_r1i1p1_CLMcom-CCLM4-8-17 (short: MPI rcp85)
  - ICHEC-EC-EARTH_rcp85_r12i1p1_SMHI-RCA4 (short: ICHEC rcp85)

- **WRF**: The open-source Weather Research and Forecasting Model (WRF) is a NWP, which is used for operational forecasting and research alike [9]. When provided with a domain and boundary conditions, which either can be real observations or idealised atmospheric conditions, it simulates fields with physical consistency. For research purposes, the Advanced Research WRF (ARW) configuration is used, which in addition to a specific solver, encompasses physics schemes, numeric and dynamics options, initialisation routines, and a data assimilation package [9]. WRF was used to simulate foehn wind fields, which then were used as fingerprint for other detected foehn cases. The WRF model was driven with the ECMWF-Integrated Forecasting System (ECMWF-IFS) at 9 km resolution.
- **TAWES weather stations**: The semi-automatic weather stations (TAWES) are a dense network of meteorological measurement sites operated by ZAMG [46]. Hourly values of pressure, temperature and wind as well as location information of several stations in Western Austria were used to create a machine learning training data set using OFC.
- **INCA**: ZAMG's Integrated Nowcasting through Comprehensive Anaylsis (INCA) is an analysis and nowcasting system, which uses all available model and observation data in Austria to supply a reliable analysis to forecast hourly instantaneous variables [6, 7]. The projected horizontal grid size is 1 km for the whole of Austria and the surrounding Alpine area. The ground wind field of INCA is generated by interpolating from a larger scale weather model and subsequent correction with observations, and afterwards adjusting the wind to the topography [7]. INCA's ground wind speed was compared to the foehn climatologies created within this thesis. The INCA wind speed has its flaws at mountain tops and in valleys, where unrealistic values are generated, which are too high on mountains and too low in valleys.

- **Station-interpolated wind field**: In the course of the same project this thesis originated from, daily wind fields generated from spatially interpolated station data for the historic time starting from 1961 were created by Tatiana Klisho MSc using Ridge Regression [8, 47]. The projected horizontal grid size is 250 m. The historic data set was then projected into the future by bias correcting EURO-CORDEX surface wind with the historic period using quantile delta mapping [48]. Like INCA, this wind field was used to compare wind speeds on foehn days. This station-interpolated wind field with replaced foehn days using WRF simulated fingerprints was the desired data outcome of this thesis.

3.2. Method Overview

An overview of how the wind climatologies including foehn occurrences were produced is given in fig. 3.1. A training data set yielding region-separated, daily information about foehn occurrence was created using weather station data from ZAMG's TAWES stations. An XGBoost algorithm was then applied on this training data for supervised learning [30]. Selected ERA5 reanalysis variables were used as input data. The trained algorithm was further applied on three selected EURO-CORDEX models to analyse foehn occurrence in the future. Simulated, physically consistent WRF ground wind fields were used to replace the station-interpolated wind field on detected foehn days, yielding the output wind field on a 250 m spatial grid. In the following sections, the the individual processes are described in more depth.

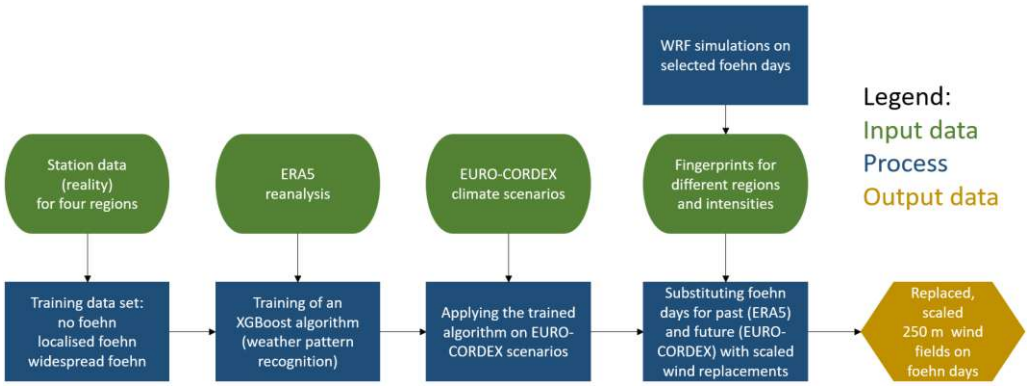

Figure 3.1.: *Overview flowchart of the methodology used to create foehn climatologies. Input data is displayed in green shapes, while processes are blue and the final output data is coloured yellow.*

3.3. Training Data Set

To be able to train a supervised machine learning algorithm like XGBoost, which detects foehn by analysing synoptic weather patterns, the creation of a training data set was required. For that purpose, Western Austria was divided into four regions, as can be seen in fig. 3.2. Selected stations within one region of the plot were attributed together and are listed in table 3.1. The regions Vorarlberg, Tiroler Oberland and Tiroler Unterland are prone to south foehn, whereas Osttirol is affected by north foehn. The training data was constructed to contain region-wise and daily information, if foehn occurred and if it was a localised or widespread event within a region.

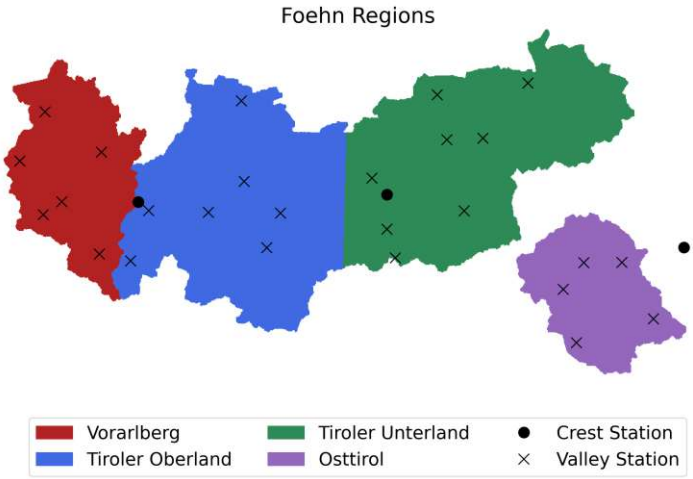

Figure 3.2.: *Foehn regions. Regions are coloured differently and their names are displayed in the legend. Crest (valley) stations are marked with black dots (crosses) and are listed in table 3.1. Osttirol's selected mountain station, visible on the the right edge of the plot is geographically located in Carinthia.*

Eleven years of consistent, hourly data TAWES weather station data from 2011-2021 were used to apply OFC on [18, 19, 46]. The stations were selected by data availability in the training period and their location close to known foehn slopes or in the typical outlet of foehn air masses. As Patscherkofel is a famous foehn affected station and close to the border between Tiroler Oberland and Unterland, it was used as crest station for both. Sonnblick, the only available crest station suitable for Osttirol is geographically located in Carinthia. Because of the lack of alternatives for crest stations in Vorarlberg, pressure values for Valluga were calculated from Galzig, which is in close proximity about 700 m below Valluga by applying the barometric height formula and considering a linear temperature gradient [14]:

$$p_V(t) = p_G(t) \cdot (1 - a(t) \cdot \frac{h_V - h_G}{T_G(t)})^{\frac{Mg}{Ra(t)}}, \tag{3.1}$$

where

- $T_V(t), h_V = 2805\,\mathrm{m}, p_V(t)$ are temperature in K, station elevation in m and pressure in hPa at the Valluga station,
- $T_G(t), h_V = 2079\,\mathrm{m}, p_G(t)$ are the temperature in K, station elevation in m and pressure in hPa at the Galzig station,
- $a(t) = -\frac{T_V(t) - T_G(t)}{h_V - h_G}$ is the vertical temperature gradient,
- $M = 0.028\,96\,\mathrm{kg\,mol^{-1}}$ is the molar mass of air,
- $g = 9.807\,\mathrm{m\,s^{-2}}$ is the gravitational acceleration and
- $R = 8.314\,\mathrm{J\,K^{-1}\,mol^{-1}}$ is the universal gas constant.

To prevent the potential temperature criteria of OFC to be fulfilled unrealistically often, Galzig was removed as valley station as a consequence.

Table 3.1.: *Selected TAWES stations [46]. These stations were selected based on their location close to known foehn slopes or in the typical outlet of foehn air masses and data availability within the training period 2011-2021. Valluga pressure values where calculated using the pressure values from Galzig and the barometric height formula with a linear temperature gradient.*

Location	**Vorarlberg**	**Tiroler Oberland**	**Tiroler Unterland**	**Osttirol**
Crest	Valluga (pressure calculated from Galzig)	Patscherkofel	Patscherkofel	Sonnblick
Valley	Brand	Galtuer	Innsbruck Uni	Virgen
	Gaschurn	St. Anton/Arlberg	Jenbach	Silian
	Bludenz	Landeck	Achenkirch	St. Jakob/Def.
	Feldkirch	Imst	Kufstein	Lienz
	Dornbirn	Reutte	Alpbach	Kals
	Schoppernau	Umhausen	Mayrhofen	
		St. Leonhard/Pitztal	Steinach	

The thresholds for OFC were mainly derived from [5], where the authors used a statistical mixture model to predict a probability for foehn in the Wipp Valley. Potential temperature and wind speed values yielding high probabilities for foehn in the statistic mixture model were used as hard thresholds for OFC. The aim was to achieve similar annual occurrence for Tiroler Unterland compared to this paper. In table 3.2 the thresholds for OFC are stated. The percentiles of the windspeed are translated to the wind speeds seen in table 3.3 in the eleven years of training data (2011-2021). While Sonnblick shows higher median wind speeds, Patscherkofel yields the highest 90^{th} percentile, implying a larger spread of values.

Table 3.2.: *OFC thresholds. The thresholds were derived in comparison to a statistic mixture model in [5]. Values yielding high probability of foehn in this model were selected as hard thresholds.*

Threshold	**Value**
Crest wind speed percentile for local events	50^{th}
Crest wind speed percentile for widespread events	90^{th}
Valley wind speed [m/s]	3
Potential temperature difference (crest minus valley) [K]	[-1,3]
Wind direction on the crest [°]	±45 S (N for Osttirol)

Table 3.3.: *Wind speed interpretation of threshold percentiles for the crest stations of the four regions in the training period 2011-2021.*

Mountain Station	**Localised limit (50^{th} percentile)** m/s	**Widespread limit (90^{th} percentile)** m/s
Valluga	4.6	8.4
Patscherkofel	5.3	14.8
Sonnblick	7.2	14.0

For distinguishing between localised and widespread events, the number of affected valley stations per event was taken into account, as can be seen in table 3.4. Roughly half of the stations were expected to respond for a widespread event.

Table 3.4.: *Required number of affected stations for distinguishing foehn occurrence. More stations were used in Tirol, therefore the numbers are higher in those regions.*

Foehn Occurrence	**Vorarlberg**	**Tiroler Oberland**	**Tiroler Unterland**	**Osttirol**
localised	1	2	2	1
widespread	3	4	4	2

After analysing the hourly station data with OFC, the daily data was built by taking the strongest event within 24 hours, yielding daily information with three classes: no foehn, localised foehn and widespread foehn.

3.4. Feature Matrix

To train an XGBoost algorithm, a feature matrix is required besides the training data set. For that purpose, the ERA5 variable fields of the same days as the training data set were used over the Alpine area with the domain reaching from 44° - 50° latitude and 8° - 17° longitude in 0.25° steps. This resulted in 37 x 25 pixels.

Physical variables describing foehn, which are also stated in section 2.3 were used. Further information including their abbreviations, pressure levels and number of data points are listed in table 3.5. The day of the year was also considered to account for seasonality. To ensure cyclic behaviour, the cosine of the day of year was built. Cross-alpine pressure gradients were used as they are the strongest drivers for foehn [15]. As surface potential temperature is not reliable in coarse models due to the flattened topography and resulting effects like cold air pools, the potential temperature at 850 hPa was chosen as a tracer for foehn. To prevent unrealistic values when the pressure level occasionally lies below the topography, the surface potential temperature was used below 1200 m. Both variables were taken as cross-alpine gradient using ±1.0° latitude as references to account for model peculiarities in the lower pressure levels. One gradient was calculated for every pixel in longitude, which means, for every main ridge pixel. Wind speed and wind direction at 500 hPa were used on every available pixel by flattening the two dimensional fields to a single array. Wind resulting from foehn is having a strong component perpendicular to the ridge, which is northward and southward for the Alps in the domain longitudes. The 500 hPa geopotential difference between every pixel and the main ridge pixel on the same longitude was also used. Geopotential differences typically describe wind flow and synoptic weather patterns in general. Because foehn replaces cold air masses in the valleys with a warmed and dried air mass, relative humidity decreases [15]. To display that, the 850 hPa relative humidity difference compared to the monthly mean for every pixel above 1200 m was used.

To use the same pixels for every model (ERA5 and the three EURO-CORDEX models), a maximum topography of all the four models was built and used for filtering the valid relative humidity pixels. The selection of variables was also constrained by their availability in EURO-CORDEX models. That is why the 700 hPa level, which would have been more suitable for wind variables, was not considered.

In total, this yielded a feature matrix of the size 4018 days x 3646 variables for ERA5 during the training period. The feature matrices of the whole historic period or the future scenarios in EURO-CORDEX models have the same amount of variables but more data points.

Table 3.5.: *Feature matrix input variable summary. Variables, which physically describe foehn were selected. The second column describes, at which pressure level the variables were used. Surface potential temperature was used only below* 1200 m. *While the cross-alpine pressure and potential temperature gradient were taken once for every longitude, the other variables were taken on every valid pixel.*

Variable	**Pressure level [hPa]**	**Description**	**Number of data points**
doy [0...1]	-	Cosine of day of year	1
Δp [Pa]	sfc	Cross-alpine pressure gradient ±1.0° latitude from main ridge	37 (length of main ridge)
$\Delta\theta 850$ [K]	850 (sfc)	Cross-alpine potential temperature gradient ±1.0° latitude from main ridge	37 (length of main ridge)
$ws500$ [m/s]	500	Total wind speed	925 (every pixel)
$wd500$ [v/ws]	500	Wind direction in fraction of north wind speed component to total	925 (every pixel)
$\Delta Z500$ [m^2/s^2]	500	Horizontal geopotential difference to main ridge on same longitude	925 (every pixel)
$\Delta rh850$ [%]	850	Relative humidity difference to monthly mean	796 (every pixel above 1200 m)

3.5. Preparation of the XGBoost Algorithm

With the training data generated from station data and the feature matrix created from synoptic ERA5 weather patterns using physically relevant variables, an XGBoost algorithm was used to link the training data with synoptic patterns. Two algorithms per region were trained, one deciding between no foehn and foehn and one distinguishing localised from widespread foehn. Therefore, in total eight XGBoost algorithms were trained. A hyperparameter grid search using cross validation of five random sets of the feature matrix was performed to achieve the highest accuracy. Early stopping and balanced class weightings were used. The hyper parameters yielding the algorithms with the best accuracy are given in appendix A.2.

3.6. WRF Simulated Fingerprints

For the WRF simulated foehn cases, the settings shown in table 3.6 were used. Three one-way nested domains of the grid size 3 km, 1 km and 300 m were used to save calculation time as can be seen in fig. 3.3. The domain with the finest resolution covers all four foehn regions and was regridded bilinearly to the desired output grid with a grid size of 250 m after simulation. Runs were always started at the beginning of the first day to ensure a proper up-cycling phase. The WRF simulations were conducted by Katharina Perny MSc.

For simulating base wind field fingerprints during foehn events, the dates visible in table 3.7 were chosen. These foehn events occurred within the training period and appeared in the results of the training data set. For every region one local and one widespread foehn was simulated to cover a variety of physically possible foehn scenarios. One instantaneous ground wind field was selected as base fingerprint for every physically possible combination, for example foehn being widespread in Vorarlberg, localised in Tiroler Oberland and Tiroler Unterland and not occurring in Osttirol. Instantaneous and not daily mean wind fields were chosen because the required calculation time to generate one mean field for every possible combination was not feasible within the project's time span. By simulating selected cases and afterwards using different time steps for diverse stages of foehn build-up with altering affected regions and intensities, the calculation time was reduced dramatically. As a drawback, a conversion from instantaneous to daily mean had to be performed afterwards, which is described in the next section. The table yielding information, which instantaneous hour for which combination of foehn occurrence was selected, is visible in appendix A.1.

Table 3.6.: *WRF settings and parameterization schemes used to run the foehn events. [9]*

Physical parameterization	**Scheme**
Shortwave/longwave radiation	Rapid Radiative Transfer Model for GCM application (RRTMG)
Microphysics	WRF Single-Moment 6-Class Microphysics (WSM6)
Planetary Boundary Layer (PBL)	Mellor-Yamada-Janjic (MYJ)
Land-Surface Model (LSM)	Noah
Cumulus	None

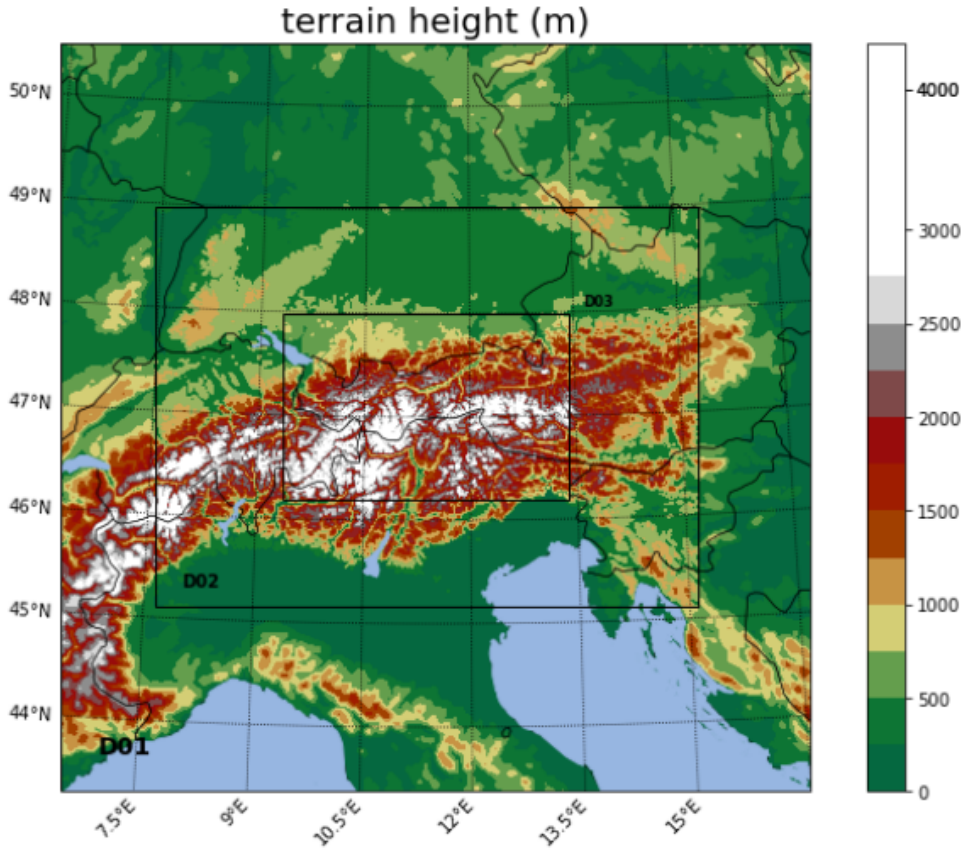

Figure 3.3.: *WRF domains. Three one-way nested domains with a pixel size of* 3 km *(D01),* 1 km *(D02) and* 300 m *(D03) were used. The finest domain covers all four foehn regions. The colourbar describes the terrain height of the model in metres.*

Table 3.7.: *Selected dates for WRF simulation. Events, which also were detected within the training period using OFC were chosen and selected in a way, that every region had at least one local and one widespread event.*

Region	**Localised**	**Widespread**
Vorarlberg	2017-02-27 10:00 - 2017-02-28 23:00	2017-03-03 07:00 - 2017-03-04 23:00
Tiroler Oberland	2020-10-21 12:00 - 2020-10-21 17:00	2017-12-10 22:00 - 2017-12-12 15:00
Tiroler Unterland	2016-09-15 08:00 - 2016-09-16 14:00	2020-10-02 00:00 - 2020-10-03 15:00
Osttirol	2018-11-26 23:00 - 2018-11-28 05:00	2017-10-28 07:00 - 207-10-30 16:00

3.7. Fingerprint Scaling

After generating the base fingerprints using selected WRF simulated foehn ground wind fields, scaling was applied for covering a variety of foehn events with individual intensities. First, the hourly training data was compared to the full hours of the WRF simulations. The hours on which a region was affected by foehn according to the training data were used to generate a pixelwise linear regression between the 500 hPa WRF wind speed $w_{500,\mathrm{FP}}$ and the ground wind speed $w_{\mathrm{g,FP}}$:

$$w_{\mathrm{g,FP,reg}} = k \cdot w_{500,\mathrm{FP}} + d\,, \tag{3.2}$$

where the slope k was calculated and $d = 0$ was set as condition for the intercept. Afterwards the relative root mean square error (relative RMSE)

$$\varepsilon = \sqrt{\sum 1 - \frac{k \cdot w_{500,\mathrm{FP}}}{w_{\mathrm{g,FP}}}} \tag{3.3}$$

was calculated for very pixel. Fig. 3.4 shows the results for the regression. In the top plot, the slope k is displayed, showing a trend of steeper slopes in higher elevations. The relative RMSE ε is shown in the middle, following the trend of k. An analysis of how linear dependent the two wind speeds are to each other is given by the Pearson correlation coefficient in the bottom plot [49]. The closer to 1 (-1), the higher is the positive (negative) linear correlation of two variables.

To convert the instantaneous WRF simulated fingerprint into daily wind fields, a conversion factor f was calculated. For every fingerprint the relation between the instantaneous wind speed of the corresponding pixel and the daily mean of every active TAWES station was built. Only values smaller than two were considered to assure, that model and station were in the same foehn regime. The calculated factors per fingerprint are displayed in fig. 3.5. The individual factors per fingerprint were averaged to account for different foehn event lengths, yielding

$$f = 0.570 \pm 0.127\,, \tag{3.4}$$

as conversion factor between instantaneous and daily wind fields.

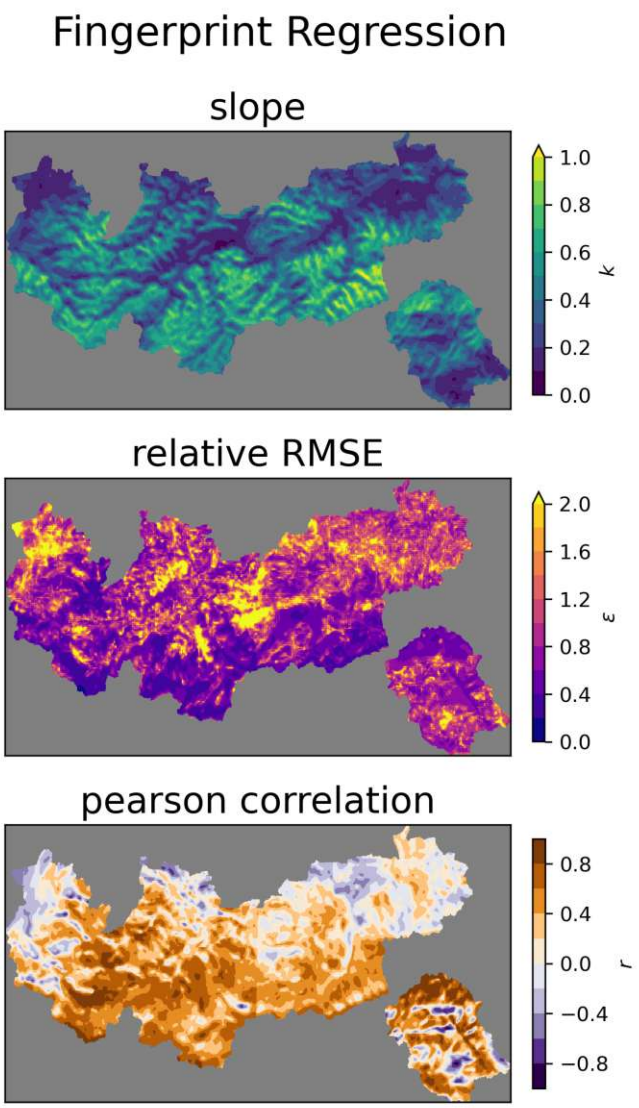

Figure 3.4.: *Regression between* 500 hPa *wind speed and ground wind speed of the fingerprints during foehn hours. Regression was performed pixelwise with no intercept, yielding the dimensionless slope k (top), the dimensionless relative RMSE ε (middle) and the Pearson correlation coefficient r (bottom).*

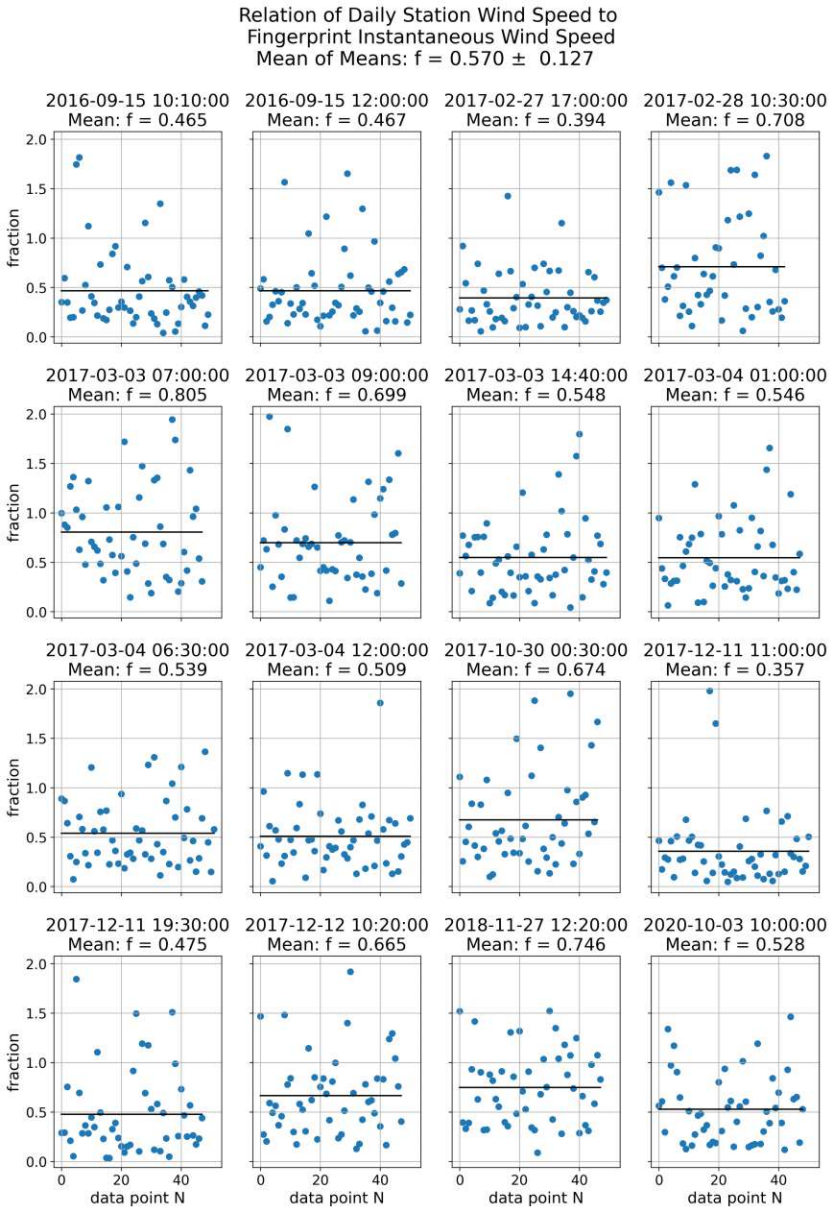

Figure 3.5.: *Instantaneous WRF simulated windspeed to daily station mean wind speed relations for every fingerprint. The horizontal axis describes the data points of active stations during the foehn event. The vertical axis describe the fraction of instantaneous WRF simulated windspeed to daily station mean wind speed (limited to 2). Mean of individual fingerprints are visible in the subplot title and indicated by black lines. To account for different foehn event lengths, the factor was averaged across all fingerprints to the value visible in the header.*

The slope k was used together with the relation κ between the 500 hPa model and fingerprint wind speed to scale the fingerprint. The relative RMSE ε was used to put a statistical noise on the fingerprint by generating a random number $r \in [-1, 1]$. The instant to daily factor f was used to convert the instantaneous fingerprint into daily wind speed replacements. Combined this reads as follows:

$$w_{\mathrm{g}} = w_{\mathrm{g,FP}} \cdot f \cdot (1 + r \cdot \varepsilon + \kappa \cdot k)\,, \tag{3.5}$$

where a description the variables is given in table 3.8. Hereby $w_{\mathrm{g,FP}}$ and w_{g} were limited by a cutoff at 50 m/s. κ was restricted to 3 and the product $\kappa \cdot k$ to -1 in the negative range to prevent negative wind speed values.

Table 3.8.: *Scaling variables used to convert the WRF-simulated fingerprint into a daily wind field during foehn days. Variables were applied either for every pixel of the project domain or as one value for the whole domain.*

Variable	**Description**	**Location**
w_{g} [m/s]	Resulting ground wind speed	pixelwise
$w_{\mathrm{g,FP}}$ [m/s]	Initial WRF simulated ground wind speed of the fingerprint	pixelwise
$r \in [-1, 1]$ [-]	A random, gaussian distributed number ($\mu = 0, \sigma = \frac{1}{3}$) determined once per fingerprint	domain-wide
ε [-]	Relative RMSE	pixelwise
$\kappa = \max(\frac{w_{500,\mathrm{m}}}{w_{500,\mathrm{FO}}}, 3)$ [-]	Fraction between 500 hPa windspeed of the models (ERA5, EURO-CORDEX, daily mean) and the WRF-fingerprint (instantaneous), maximum of 3	pixelwise
k [-]	Slope of linear regression $y = k \cdot x + d$ with intercept $d = 0$ between WRF 500 hPa and ground wind speed	pixelwise
$f = 0.570$ [-]	Factor describing relation between instantaneous fingerprint wind speed and daily station mean	domain-wide

Similar patterns for foehn with different absolute wind speeds were generated with this scaling procedure.

3.8. Applying the XGBoost Algorithm and Fingerprints

The XGBoost algorithms trained with eleven years of ERA5 variables and data generated from OFC were afterwards applied to the full time range of ERA5 and the three EURO-CORDEX models. For every detected foehn day, a fingerprint corresponding to the affected regions was selected, scaled and used as replacement for existing station-interpolated wind fields. For determining if a pixel was affected by a foehn event, a wind speed condition was applied, where the OFC threshold for valley winds was multiplied by the instant-to-daily factor f:

$$\text{cond} = 3\,\text{m/s} \cdot f = 1.71\,\text{m/s}\,. \tag{3.6}$$

The station-interpolated wind field containing replaced foehn patterns and the affected pixels per foehn day marked the desired outcome of the project [8].

4. Results and Discussion

4.1. Training Data Set Results

By applying OFC to hourly TAWES stations and afterwards taking the strongest event per day, a daily foehn training data set was created. The results of the training data set are given in table 4.1. The seasonality of the occurring foehn days for the eleven training years is visible in fig. 4.1. In midsummer and midwinter, where air flows are predominantly static, less foehn is observed while in spring foehn occurrences are peaking in all four regions. Osttirol has a less pronounced seasonality trend than the other, south foehn affected regions.

The regions have a foehn occurrence of 11 - 18 %. Tiroler Unterland yields the highest foehn occurrence as well as the highest percentage of widespread events. One explanation could be, that the Wipp Valley displays an ideal valley for foehn events, with pronounced foehn occurrences, which are centre of several studies [19, 20, 21]. The results in Tiroler Unterland are in good agreement with [5]. The rest of the percentages were validated by foehn experts from Innsbruck, Austria [50]. Stations in close vicinity of the Alps' main ridge responded most frequent, which was expected because foehn has the highest probability of descending in these locations.

Table 4.1.: *Foehn occurrence in the training data set. The results are given in percent of one year's days (an average of 365.25) as well as average days per year and are divided between localised and widespread foehn. These two categories differ in the number of affected stations and wind speed at the mountain station.*

	Vorarlberg	**Tiroler Oberland**	**Tiroler Unterland**	**Osttirol**
localised foehn				
[%]	10.6	14.2	13.4	13.1
[avg. days per year]	38.7	51.9	49.1	48.0
widespread foehn				
[%]	1.2	1.0	4.5	1.0
[avg. days per year]	4.4	3.5	16.6	3.7
sum				
[%]	11.8	15.2	17.9	14.1
[avg. days per year]	43.1	55.4	65.7	51.7
most responding station	Brand	Galtuer	Steinach	Kals

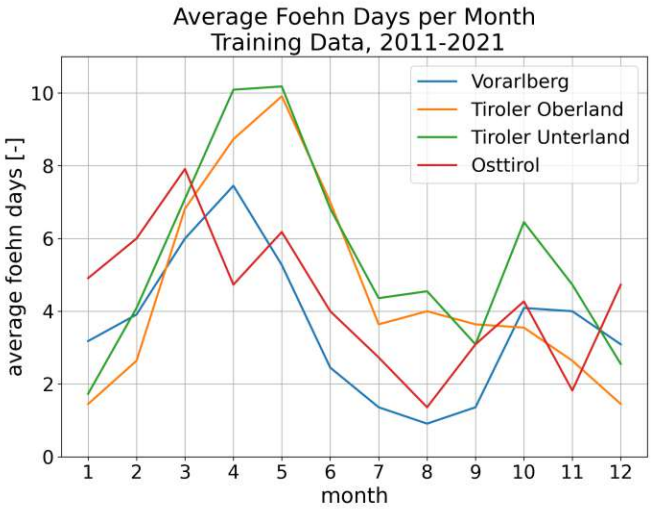

Figure 4.1.: *Seasonality of foehn days in the training data set. Regions are colour-coded and visible in the legend. The horizontal axis describes the months of the year, the vertical axis the accumulated average foehn days on monthly basis.*

4.2. XGBoost Algorithm Performance

In total eight XGBoost algorithms were trained, two for every region, one classifying between foehn and no foehn and one deciding if the event is localised or widespread. The hyperparameters yielding the best predictions per algorithm are displayed in appendix A.2. The training accuracies of the algorithms are displayed in table 4.2 and table 4.3.

For deciding between foehn and no foehn, the accuracy exceeds 95 % in all regions. Besides Osttirol, where the false alarms outweigh the missed events by nine days, all other false alarms are within two days compared to the missed events. This indicates that the synoptic patterns for north foehn Osttirol are difficult to distinguish from other weather pattern.

When classifying, if an event is localised or widespread, the accuracies are also above 95 % for Vorarlberg, Tiroler Oberland and Osttirol. The algorithm in Tiroler Unterland fails to be as accurate and misses 37.7 % of the widespread events. This indicates that the events in Tiroler Oberland are harder to distinguish from one another, meaning that either the synoptic patterns are similar or the training data thresholds in Tiroler Unterland were set insufficiently restrictive.

Table 4.2.: *Accuracy of the XGBoost Algorithms deciding between foehn or no foehn occurrence. The values in percent and average days per year are given in relation to the total members of the respective class. The positive class hereby indicates foehn, the negative no foehn.*

YES/NO	Vorarlberg	Tiroler Oberland	Tiroler Unterland	Osttirol
Accuracy				
[%]	97.7	97.6	98.3	95.7
[avg. days per year]	356.8/365.25	356.5/365.25	359.0/365.25	349.5/365.25
True Positives				
[%]	90.9	92.0	96.7	93.5
[avg. days per year]	39.2/43.1	51.00/55.4	63.5/65.7	48.4/51.7
True Negatives				
[%]	98.6	98.6	98.7	96.1
[avg. days per year]	317.5/322.2	305.4/309.8	295.6/299.5	301.2/313.5
Missed Events				
[%]	9.1	8.0	3.3	6.5
[avg. days per year]	3.9/43.1	4.4/55.4	2.2/65.7	3.4/51.7
False Alarms				
[%]	1.4	1.4	1.3	3.9
[avg. days per year]	4.6/322.2	4.4/309.8	3.9/299.5	12.4/313.5

Table 4.3.: *Accuracy of the XGBoost Algorithms deciding between localised and widespread foehn. The values in percent and average days per year are given in relation to the total members of the respective class. The positive class hereby indicates widespread, the negative localised foehn.*

LOCALISED/WIDESPREAD	Vorarlberg	Tiroler Oberland	Tiroler Unterland	Osttirol
Accuracy				
[%]	96.4	99.0	84.1	96.8
[avg. days per year]	352.1/365.25	361.6/365.25	307.2/365.25	353.6/365.25
True Positives				
[%]	95.8	87.2	62.3	92.7
[avg. days per year]	4.2/4.4	3.1/3.5	10.4/16.6	3.4/3.7
True Negatives				
[%]	96.5	99.8	91.5	97.2
[avg. days per year]	37.4/38.7	51.8/51.9	44.9/49.1	46.6/48.0
Missed Events				
[%]	4.2	12.8	37.7	7.3
[avg. days per year]	0.2/4.4	0.4/3.5	6.3/16.6	0.3/3.7
False Alarms				
[%]	3.5	0.2	8.5	2.8
[avg. days per year]	1.4/38.7	0.1/51.9	4.2/49.1	1.4/48.00

To assess if the algorithms learned to take into account physical meaningful variables during training, the importance of a feature for a classification was observed. Fig. 4.2 and 4.3 show two examples of the top 20 important features for Tiroler Unterland for classifying between foehn and no foehn and between localised and widespread foehn. As the relative feature importance sums up to one, values close to 0.1 impose a significant part of the decision. In the bar graphs, it can be seen that the importance rapidly decreases after the first several features. In table 4.4 the most important features for every XGBoost algorithm are listed.

Table 4.4.: *Most important XGBoost features of every algorithm. Loc and wide are short forms of localised and widespread. Features are given in abbreviations visible in table 3.5 and are attributed to a location using the pressure level (plev), latitude (lat) and longitude (lon). Relative importance sums up to one for all features.*

Algorithm	**Feature [var, plev,lat,lon]**	**Relative Importance [-]**
Vorarlberg yes/no	Δp, sfc , 47.00, 12.75	0.24
Vorarlberg loc/wide	Δp, sfc , 47.00, 13.75	0.10
Tiroler Oberland yes/no	Δp, sfc, 47.00, 13.75	0.11
Tiroler Oberland loc/wide	wd, 500, 48.00, 11.75	0.22
Tiroler Unterland yes/no	Δp, sfc, 47.00, 11.75	0.06
Tiroler Unterland loc/wide	Δp, sfc, 47.25, 14.00	0.08
Osttirol yes/no	wd, 500, 47.75, 8.00	0.07
Osttirol loc/wide	$\Delta\theta$, 850, 46.50, 8.5	0.14

The most important features either are cross-alpine pressure gradients, potential temperature gradients or wind directions. It is reasonable, that cross-alpine pressure gradients would be the most important features in most cases as they are drivers of foehn. Noteable is the dislocation of the features - all most important features except in the algorithm of Tiroler Unterland distinguishing between no foehn and foehn are not located in the corresponding regions. The cross-alpine gradient in the area of Salzburg and Carinthia gives the most prominent information about foehn in Vorarlberg, while the wind direction and potential temperature gradient in Switzerland indicates north foehn in Osttirol.

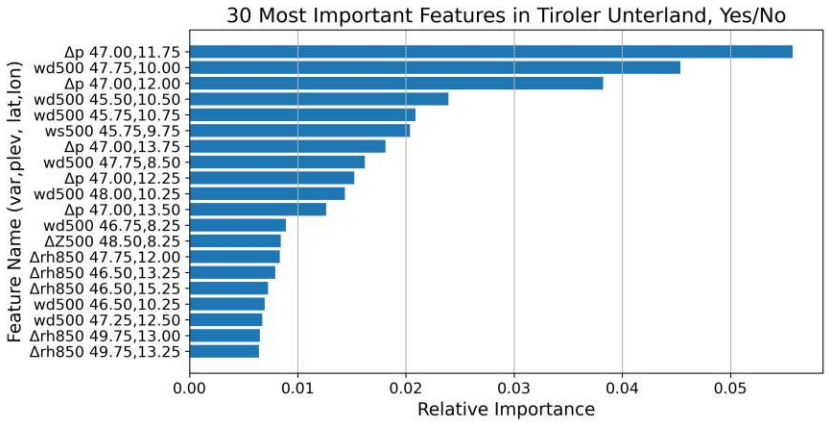

Figure 4.2.: *Feature importance of Tiroler Unterland's XGBoost algorithm for classifying between foehn and no foehn. The relative importance visible in the horizontal axis sums up to one. Variables are stated in the vertical axis with the variable name, followed by the pressure level (plev), latitude (lat) and longitude (lon). The variables are either describing a cross-alpine gradient in the case of* Δp *and* $\Delta\theta 850$ *or a value at a single latitude-longitude pixel. For a variable description refer to table 3.5.*

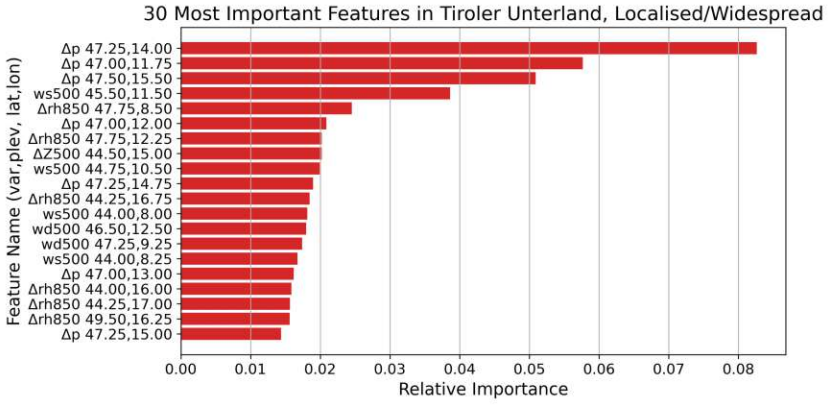

Figure 4.3.: *Feature importance of Tiroler Unterland's XGBoost algorithm for classifying between localised and widespread foehn. The relative importance visible in the horizontal axis sums up to one. Variables are stated in the vertical axis with the variable name, followed by the pressure level (plev), latitude (lat) and longitude (lon). The variables are either describing a cross-alpine gradient in the case of* Δp *and* $\Delta\theta 850$ *or a value at a single latitude-longitude pixel. For a variable description refer to table 3.5.*

4.3. Application on Climate Models

The algorithms were applied on the historic period (1991-2020) of the ERA5 reanalysis and the three EURO-CORDEX climate models after analysing the accuracy during the training period. The climate models' ability to produce similar synoptic patterns representing possible foehn days can be assessed by comparing the foehn occurrence and distribution of localised and widespread events in table 4.5 as well as foehn seasonality in the historic period in fig. 4.4.

The ERA5 reanalysis shows good agreement with the training data set in the south foehn regions. While the EURO-CORDEX models tend to underestimate foehn days in general by up to two days per month yielding smaller occurrences by up to 2.5 %. In the three south foehn regions, the foehn occurrences are therefore more alike compared to the training data set than for the north foehn region Osttirol. The seasonal trend is also conserved in all south foehn regions. North foehn in Osttirol does not have a pronounced seasonality in the climate models as well. North foehn occurs more often during summer in the MPI models indicating, that the XGBoost algorithms have difficulty to separate north foehn from other phenomena like Atlantic storms in these models. The missing seasonal trend for Osttirol is an indicator, that south foehn as a pre-frontal phenomenon is better recognisable in synoptic pattern than the post-frontal north foehn in the EURO-CORDEX models. The less pronounced seasonality of ERA5 and EURO-CORDEX models for north foehn in Osttirol therefore suggest, that the models fail to predict the correct trace of low pressure centres. Distinguishing between localised and widespread foehn is yielding satisfying results, only exceeding 1 % difference for Tiroler Unterland.

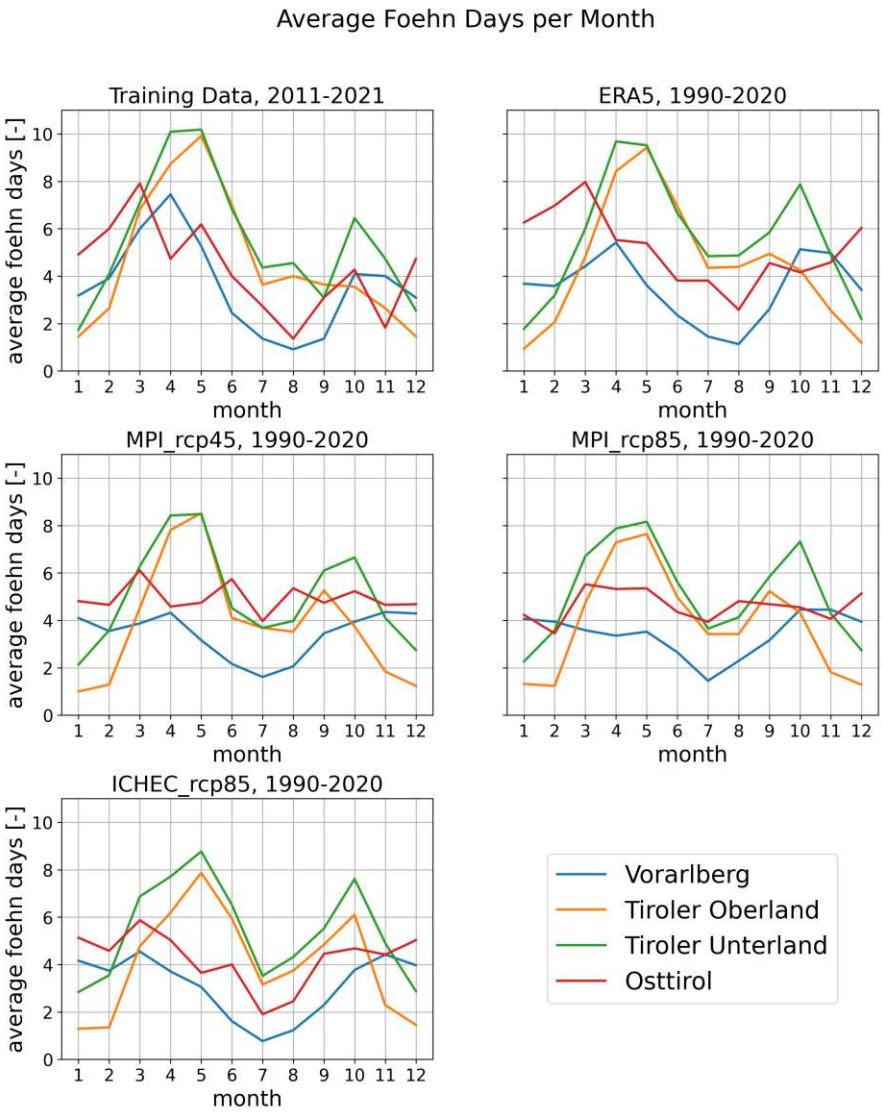

Figure 4.4.: *Comparison of foehn seasonality between models. Regions are colour-coded and visible in the legend. The horizontal axis describes the months of the year, the vertical axis the accumulated average foehn days on monthly basis. Model names are stated in the title of the subplots. While the training period is 2011-2021, model seasonality is displayed over the whole historic reference period (1990-2020) for more statistic relevance.*

Table 4.5.: *Comparison of foehn occurrence in the models. The results are separated for the specific regions and are given in percent of one year's days (an average of 365.25) as well as average days per year. Detected occurrences are divided between localised and widespread foehn. While the training data occurrences are given within the training period (2011-2021, first column), model occurrences are displayed over the whole historic reference period (1990-2020) for more statistic relevance, visible in column two to five.*

	Training Data (2011-2021)	**ERA5** (1990-2020)	**MPI rcp45** (1990-2020)	**MPI rcp85** (1990-2020)	**ICHEC rcp85** (1990-2020)
Vorarlberg					
localised foehn					
[%]	10.6	10.1	9.2	9.1	9.1
[avg. days per year]	38.7	36.8	33.7	33.2	33.1
widespread foehn					
[%]	1.2	1.4	2.0	2.1	1.1
[avg. days per year]	4.4	5.0	7.2	7.6	4.2
sum					
[%]	11.8	11.5	11.2	11.2	10.2
[avg. days per year]	43.1	41.8	40.9	40.8	37.3
Tiroler Oberland					
localised foehn					
[%]	14.2	14.1	12.0	11.9	12.4
[avg. days per year]	51.9	51.5	43.8	43.4	45.5
widespread foehn					
[%]	1.0	0.8	0.7	0.9	1.0
[avg. days per year]	3.5	2.8	2.7	3.3	3.5
sum					
[%]	15.2	14.9	12.7	12.8	13.4
[avg. days per year]	55.4	54.3	46.5	46.7	49.0
Tiroler Unterland					
localised foehn					
[%]	13.4	14.8	13.4	13.7	15.8
[avg. days per year]	49.1	54.1	49.1	50.2	57.8
widespread foehn					
[%]	4.5	3.6	3.2	3.3	2.0
[avg. days per year]	16.6	13.2	11.5	12.0	7.2
sum					
[%]	17.9	18.4	16.6	17.0	17.8
[avg. days per year]	65.7	67.3	60.6	62.2	65.0
Osttirol					
localised foehn					
[%]	13.1	15.6	14.5	13.7	13.1
[avg. days per year]	48.0	57.0	53.1	50.0	47.7
widespread foehn					
[%]	1.0	1.3	1.7	1.5	0.9
[avg. days per year]	3.7	4.6	6.1	5.4	3.4
sum					
[%]	14.1	16.9	16.2	15.2	14.0
[avg. days per year]	51.7	61.6	59.2	55.4	51.1

4.4. Replacement Wind Field Analysis

Fig. 4.6 shows the scaling process for the 3rd of March 2017, the date also shown in chapter 1. The original fingerprint occurred one day afterwards, visible in the top plot. By applying the scaling process from section 3.7 to the instantaneous WRF fingerprint, the replacement wind field in the middle with the pixels on the bottom satisfying the wind speed condition in equation 3.6 was obtained. The majority of pixels in the south foehn regions are affected by foehn. While not the exact same wind speed pattern as in fig. 1.3 is generated, a similar wind field with less elevation dependency is produced. Fig. 4.5 shows the difference of the scaled replacement and the WRF simulated mean wind field. Especially the wind speeds on mountains are not coinciding with each other. High wind speeds can be observed on different mountains. Valley wind speeds and the total spatial mean are similar to each other. Patterns of a single foehn event cannot be reproduced.

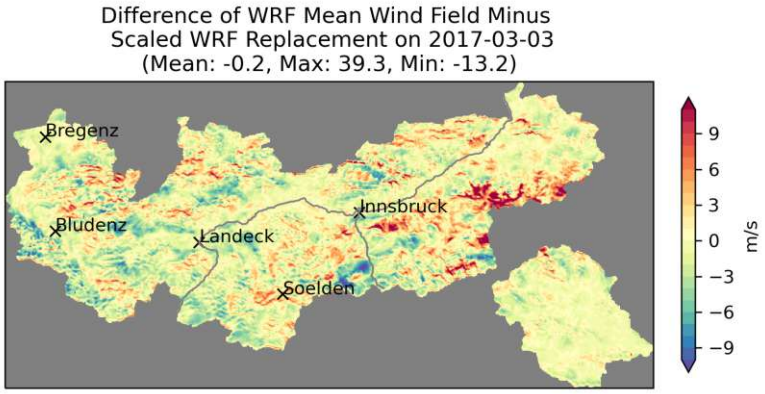

Figure 4.5.: *Difference of WRF simulated mean wind field and scaled replacements on the 3rd of March 2017. The colourbar describes differences (mean wind minus scaled replacement) of wind speed in* m/s. *Several locations are displayed with black crosses and their name for better orientation. The rivers Inn and Sill are drawn in grey lines. Mean, maximum and minimum values are calculated over the whole area.*

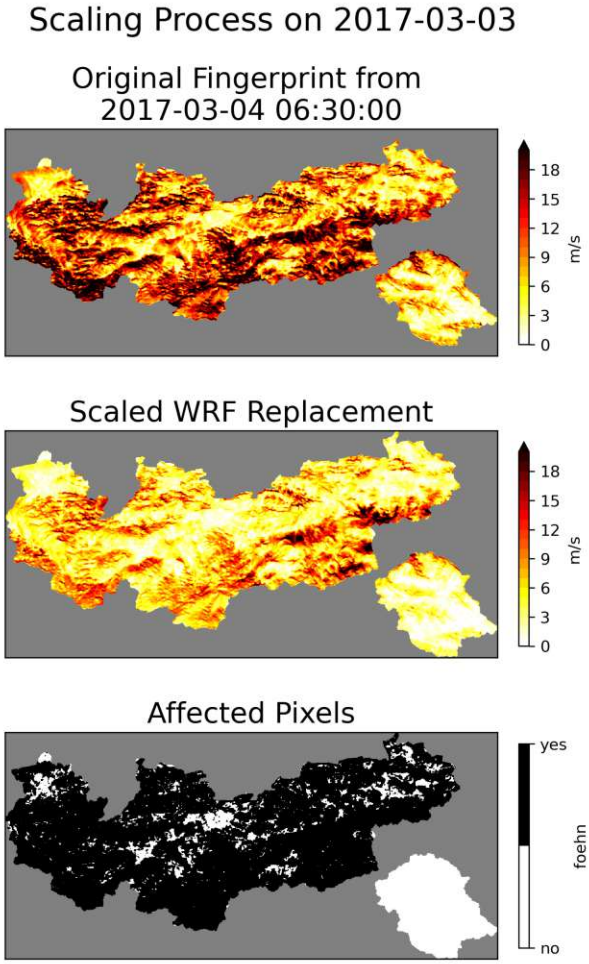

Figure 4.6.: *Scaling process for the foehn event on the 3rd of March 2017. The original fingerprint from the 4th of March 2017 (top) is scaled with the formula from section 3.7, to obtain the daily wind field replacement (middle). Both colourbars describe the same range of wind speed values in* m/s. *The pixels marked in black (bottom) are affected by foehn by satisfying the condition of having wind speeds above* 1.71 m/s.

Fig. 4.7 shows the wind climatology comparison during south foehn days of the period where INCA is available (2003-2020). The first column describes the absolute wind speed climatologies of the scaled replacements, the wind field generated from interpolated stations and ZAMG's INCA. The second column displays the difference of individual climatologies. More washed out, less elevation dependent patterns with more pronounced wind speeds in typical foehn valleys are observed for the replacements. INCA wind speed on mountains exceeds the wind speeds of the other climatologies by several m/s.

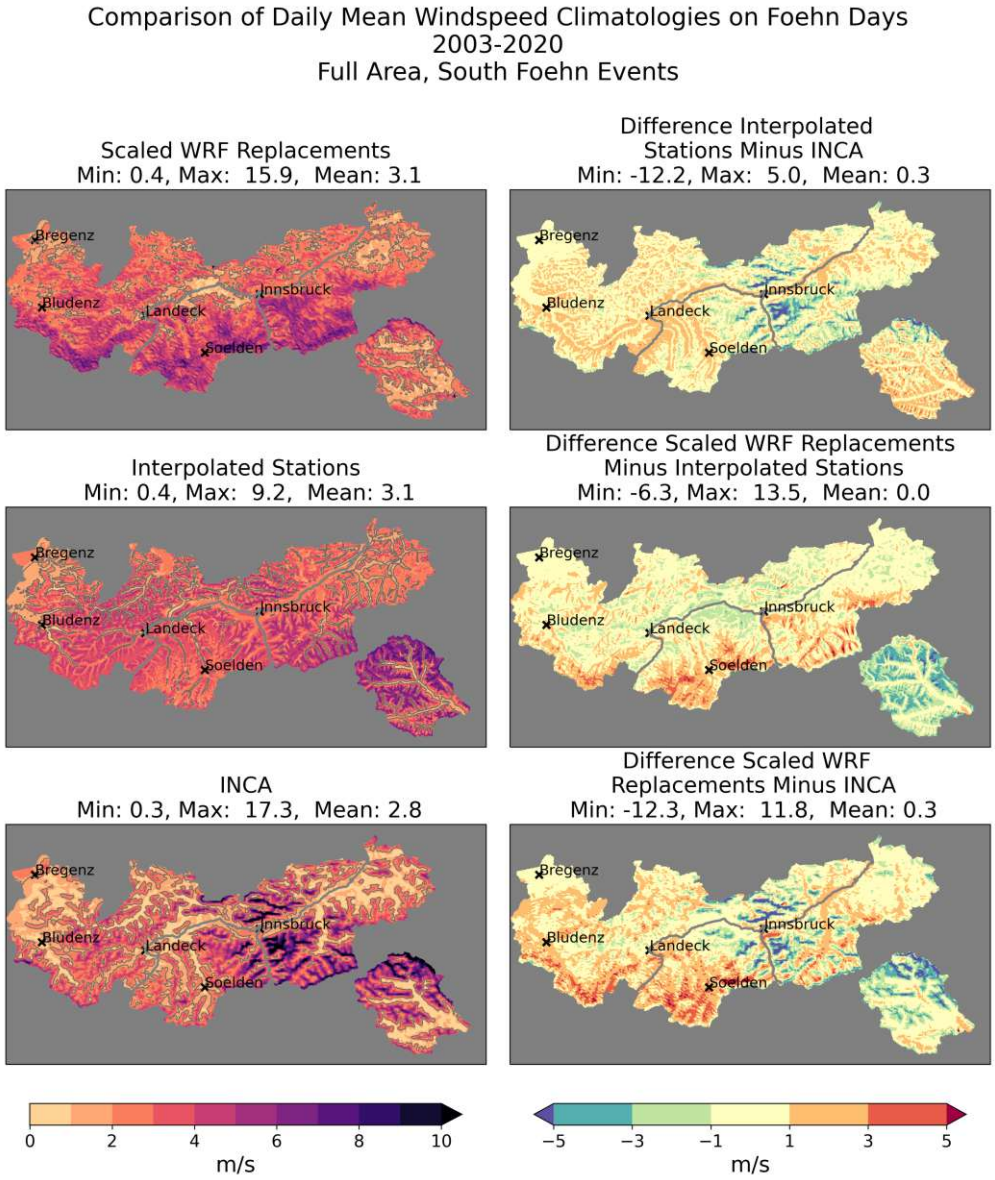

Figure 4.7.: *Spatial comparison of climatologies of south foehn days within the INCA period (2003-2020). The first column shows absolute values of wind speed climatologies in* m/s *while the second shows the difference of the individual climatologies in* m/s. *The thin grey lines in the first column show, where the wind speed condition for counting as foehn affected is satisfied. Several locations are displayed with black crosses and their name for better orientation. The rivers Inn and Sill are drawn in grey lines. Mean, maximum and minimum values are calculated over the whole area.*

Different behaviour on slopes is visible when analysing wind speeds on slopes with an inclination of over 8° during south foehn at affected pixels (fig. 4.8 and 4.9) and at foehn free pixels (fig. 4.10 and 4.11). As the Alps are almost horizontally going from west to east in Western Austria, slopes with aspects towards the north are locations, where foehn typically penetrates the valley. Higher wind speeds are observed on foehn affected pixels during south foehn for the scaled WRF replacements while the wind field generated out of interpolated stations and in INCA have similar magnitudes. Wind speeds are also higher on bulging slopes. Foehn free pixels show no distinguished direction in any of the three wind fields. Absolute values of wind speeds on foehn free pixels are the lowest for the scaled WRF replacements. Therefore, a redistribution of wind speed occurs during scaling.

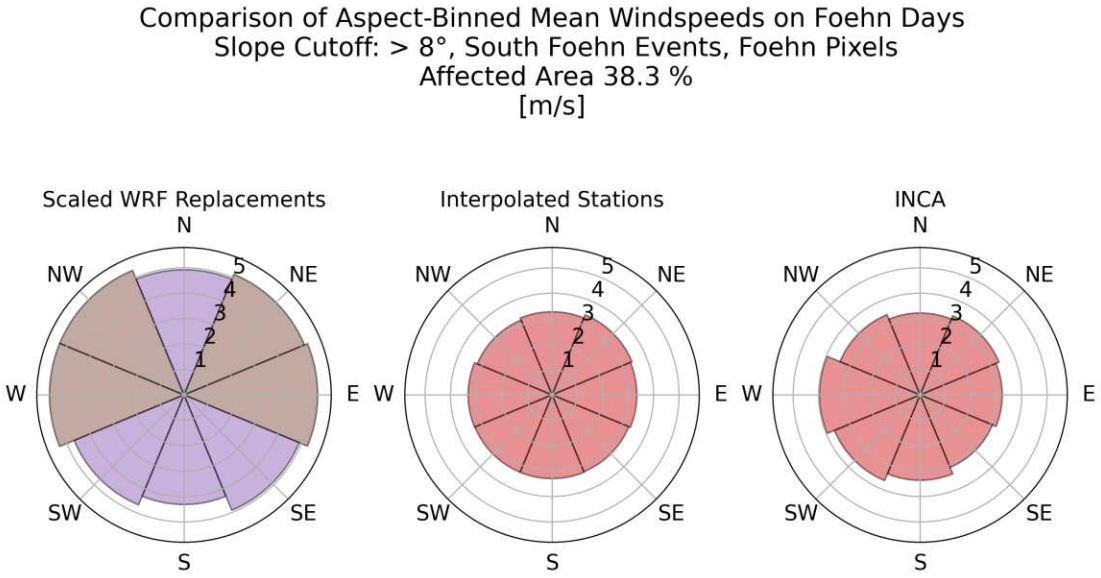

Figure 4.8.: *Wind speed climatologies at affected pixels during south foehn days, aspect binned wind roses in* m/s. *The compass directions describe where the aspect of the slopes point. One aspect covers a range of* 45°. *Matching colours are used for matching integer ranges. A total area of 38.3 % is affected by south foehn when considering slopes with inclination above* 8°.

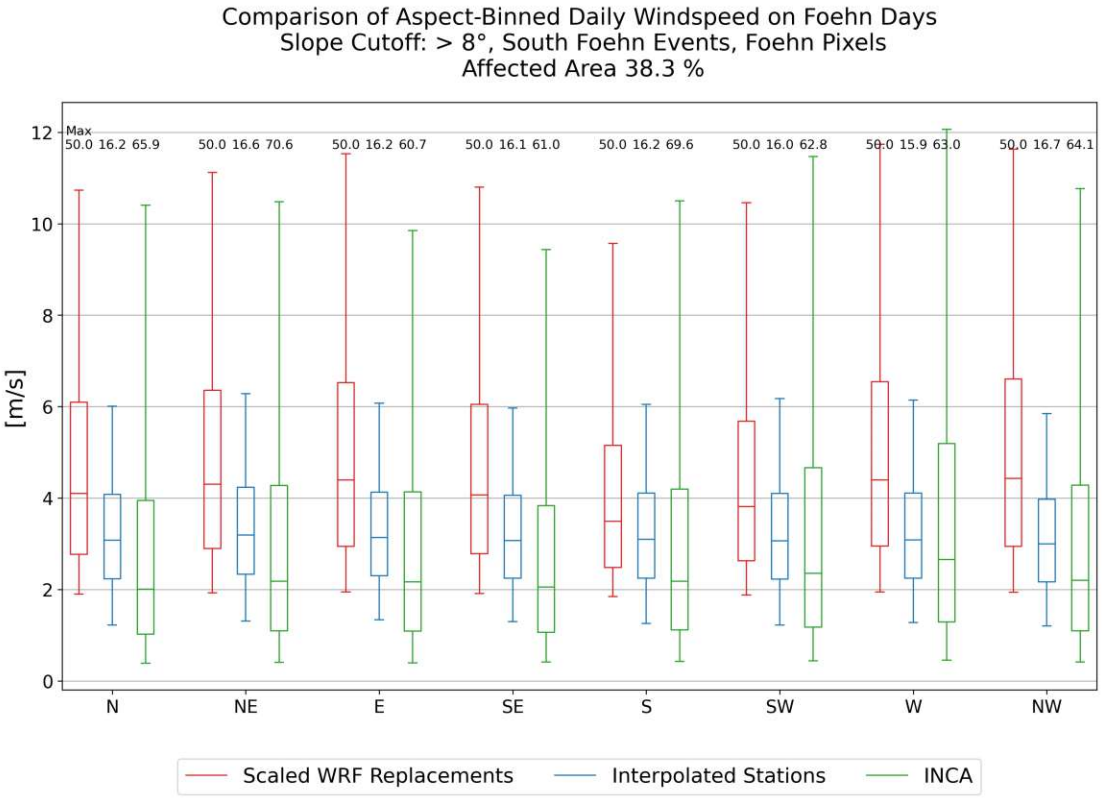

Figure 4.9.: *Wind speed climatologies at affected pixels during south foehn days, aspect binned boxplots. The compass directions on the horizontal axis describe where the aspect of the slopes point. One aspect covers a range of* 45°. *The vertical axis describes wind speeds in* m/s. *The whiskers cover the* 5^{th} *and* 95^{th} *percentile. The maxima are displayed as numbers above. A total area of 38.3 % is affected by south foehn when considering slopes with inclination above* 8°.

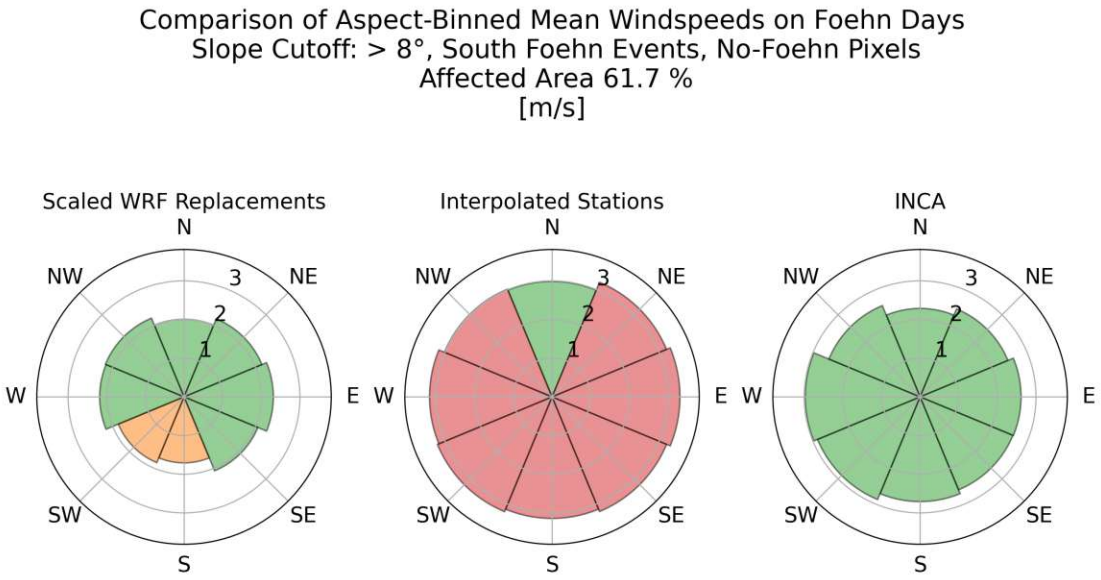

Figure 4.10.: *Wind speed climatologies at foehn free pixels during south foehn days, aspect binned wind roses in* m/s. *The compass directions describe where the aspect of the slopes point. One aspect covers a range of* 45°. *Matching colours are used for matching integer ranges. A total area of 61.7 % is not affected by south foehn when considering slopes with inclination above* 8°.

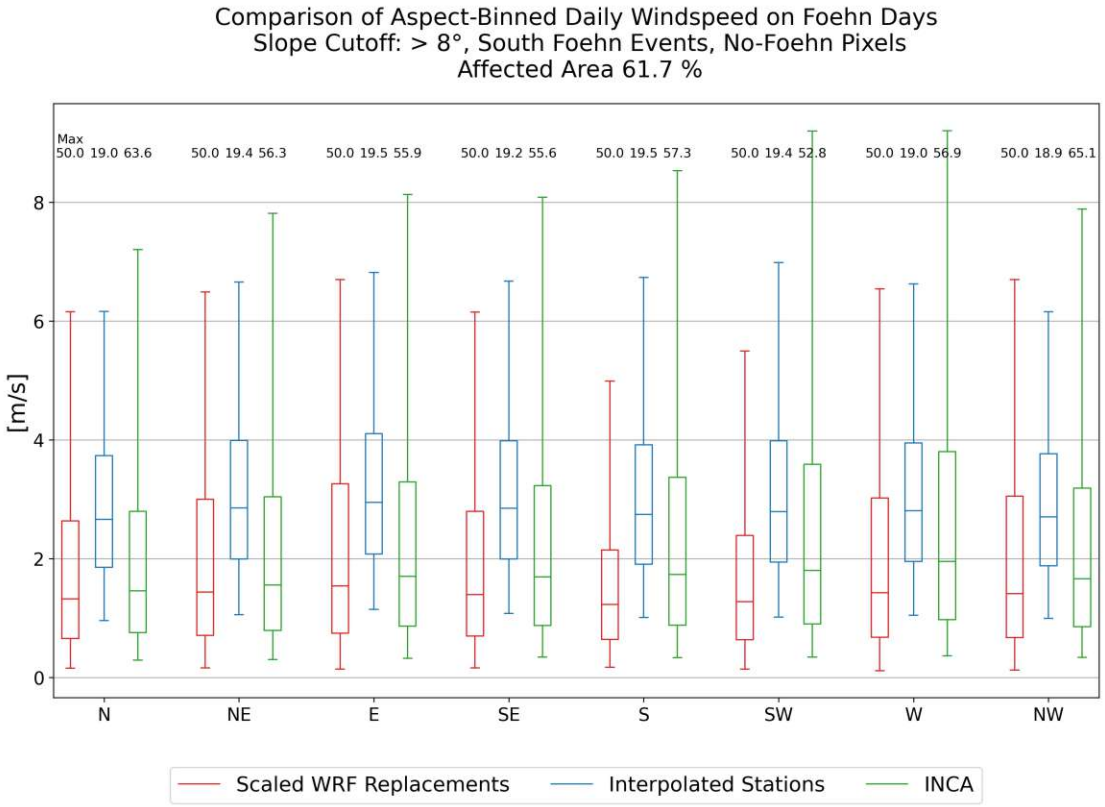

Figure 4.11.: *Wind speed climatologies at foehn free pixels during south foehn days, aspect binned boxplots. The compass directions on the horizontal axis describe where the aspect of the slopes point. One aspect covers a range of* 45°. *The vertical axis describes wind speeds in* m/s. *The whiskers cover the* 5^{th} *and* 95^{th} *percentile. The maxima are displayed as numbers above. A total area of 61.7 % is not affected by south foehn when considering slopes with inclination above* 8°.

The wind speeds at affected pixels (fig. 4.12) and at foehn free pixels (fig. 4.13) are observed binned by elevation to analyse if foehn reaches the valley during south foehn days. Clear elevation dependencies can be detected for the wind fields generated from interpolated stations and INCA. On affected pixels higher wind speeds are observed in the scaled WRF replacements for all elevations, with the highest difference in the valley elevations compared to the other wind fields. It can be concluded, that foehn reaches the valleys with higher wind speeds more often in replacement climatologies, although individual events differ from reality. On foehn free pixels a similar elevation dependency compared to the other wind fields is visible. This is the behaviour other experts desired at the start of the project [8]. The same analysis for north foehn days can be found in appendix A.3.

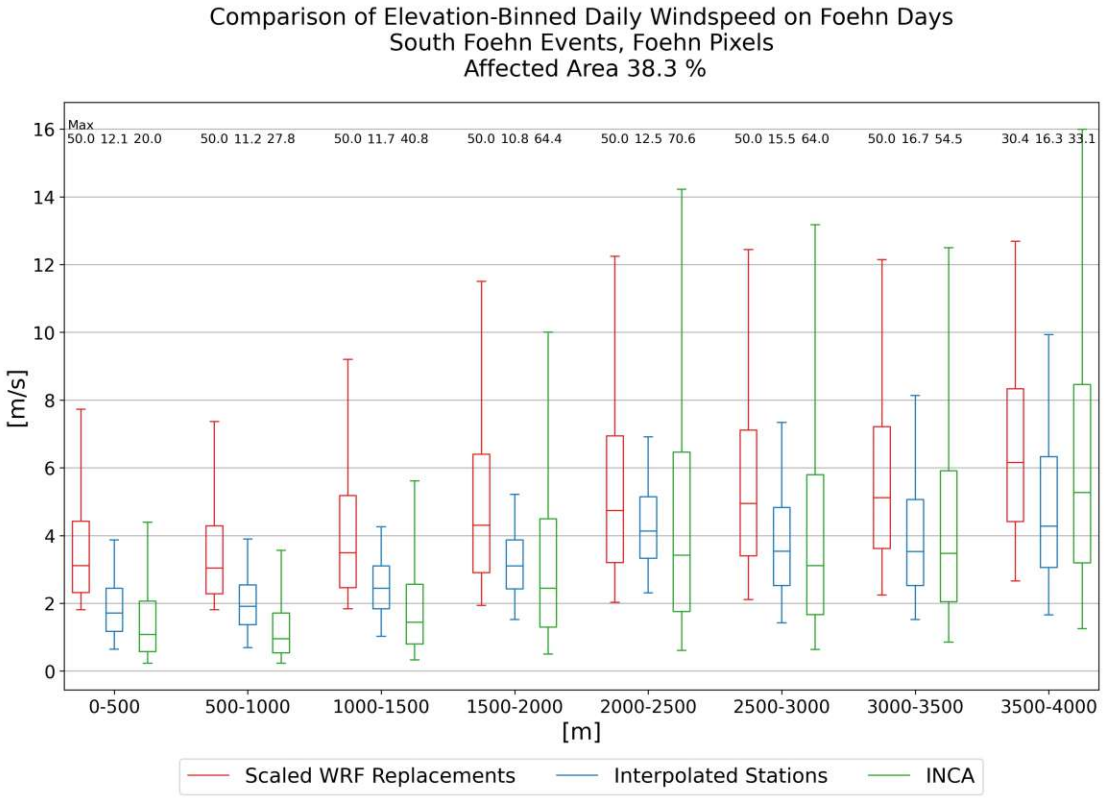

Figure 4.12.: *Wind speed climatologies at affected pixels during south foehn days, elevation binned boxplots. The horizontal axis describes elevation bins in* m. *The vertical axis describes wind speeds in* m/s. *The whiskers cover the* 5^{th} *and* 95^{th} *percentile. The maxima are displayed as numbers above. A total area of 38.3 % is affected by south foehn when considering slopes with inclination above* 8°.

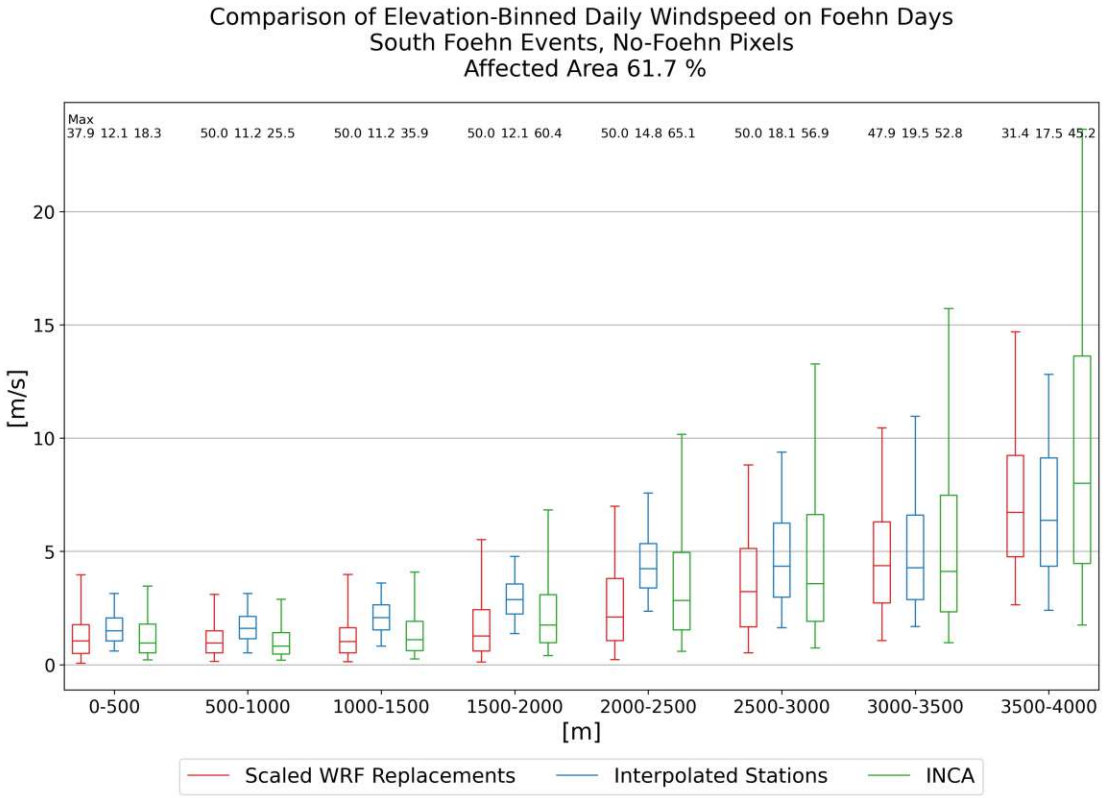

Figure 4.13.: *Wind speed climatologies at foehn free pixels during south foehn days, elevation binned boxplots. The horizontal axis describes elevation bins in* m. *The vertical axis describes wind speeds in* m/s. *The whiskers cover the* 5^{th} *and* 95^{th} *percentile. The maxima are displayed as numbers above. A total area of 61.7 % is not affected by south foehn when considering slopes with inclination above* 8°.

4.5. Development of Foehn Occurrence and Affected Pixels in Climate Models

The development of foehn occurrence in the MPI rcp85 model is analysed here, while the other two can be found in appendix A.4 and A.5. For more statistical relevance, more models of the same RCP scenario have to be analysed and set in relation to each other as described in chapter 5. In fig. 4.14 the development of foehn occurrence until 2100 for the MPI rcp85 climate model is visible. A rolling mean of 30 years is applied to smooth the curves. In this model a small negative trend in foehn occurrence is detectable towards the end of the century for all regions except Vorarlberg. The proportion of widespread events is expected to be higher except in Osttirol, where the trend is the opposite.

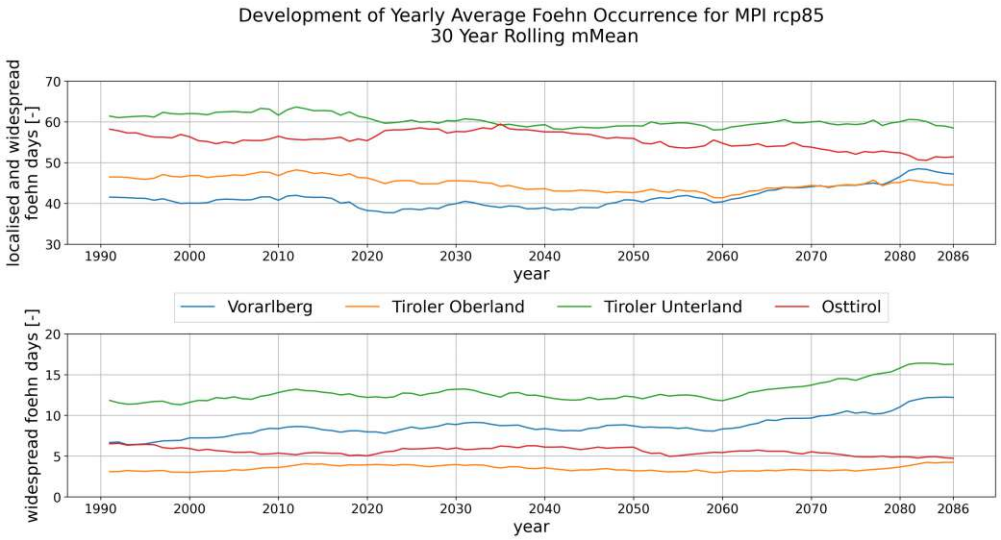

Figure 4.14.: *MPI rcp85 foehn occurrence development until 2086. The horizontal axis describes the years, while the vertical axis states average foehn days per year. The regions are colour-coded and visible in the legend. A rolling mean of 30 years is applied to smooth the curve. Because of that the last available year is 2086 as the climate models reach until 2100.*

The seasonality of the MPI rcp85 scenario visible in fig. 4.15 shows an increase in winter for the end of the century (2071-2100) in south foehn regions except Tiroler Oberland. Summer months tend to have less foehn than in the historic period indicating more stable weather patterns. Especially in Vorarlberg higher amplitudes in both directions occur by the end of the century. No clear trend for Osttirol is visible.

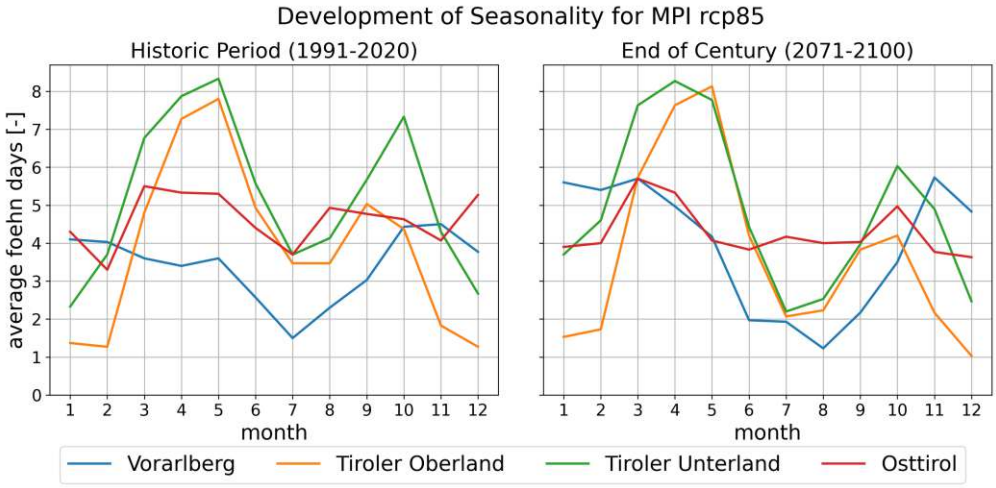

Figure 4.15.: *MPI rcp85 foehn seasonality development until 2100. Compared are the historic period (1991-2020) and the end of the century (2071-2100) of the specific model. Regions are colour-coded and visible in the legend. The horizontal axis describes the months of the year, the vertical axis the accumulated average foehn days on monthly basis.*

In fig. 4.16 the average yearly foehn days per pixel are displayed. The difference in foehn occurrence per region is clearly visible. Especially the split of Tiroler Oberland and Tiroler Unterland produces a pronounced cut between the two regions. As this artefact is not realistic, foehn days on the border of the regions have to be treated with caution. The pixels in Osttirol show a similar number as the ones in Tiroler Unterland. This is not observed in reality and can be attributed to the following reasons:

- The worse performance of the XGBoost algorithms over Osttirol predict higher foehn occurrence compared to the training data set.
- Osttirol is smaller compared to the other regions and also more elevated. Foehn occurrence results in an higher likeliness for an individual pixel to be affected, resulting in higher numbers.
- The fingerprints in Osttirol tend to produce higher wind speeds, increasing the number of affected pixels.

- Warm air typically penetrates cold valley air pools for south foehn. The penetration requires a certain amount of kinetic energy. In consequence, not every wind blowing on the crest will be classified as foehn in the valleys because it does not advect into it. For north foehn wind points in the direction of the temperature gradient. The temperature between foehn air masses and the cold air in the pools is smaller compared to north foehn, causing north foehn to advect into valleys more frequently.

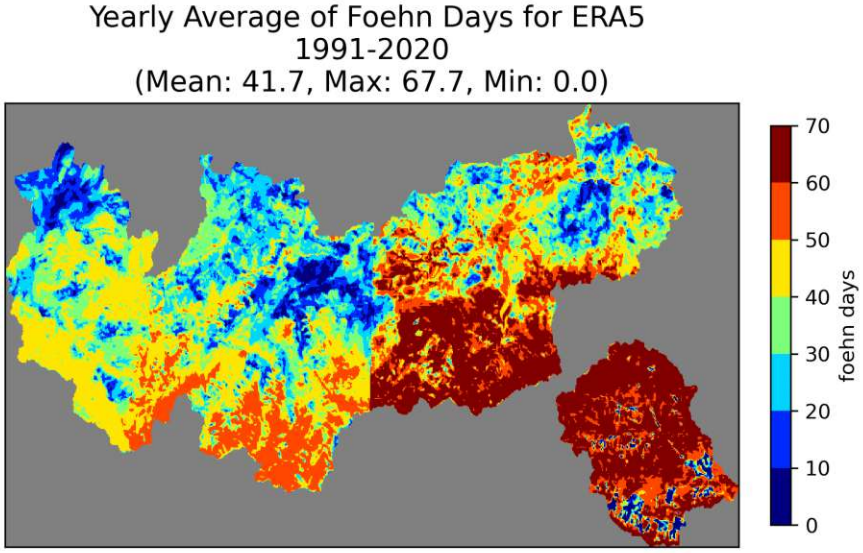

Figure 4.16.: *Average yearly foehn days per pixel in the historic ERA5 period. The colourbar describes how often a pixel is affected by foehn on yearly average in the historic period (1991-2020). Mean, maximum and minimum values are calculated over the whole area.*

The historic period in fig. 4.16 does not coincide with the climate models as they have different values within this period and therefore, fig. 4.16 is only valid for ERA5, which is closest to reality due to its reanalysis character. The differences in foehn patterns over time is distinguished by comparing the climate models' affected pixels in the historic period to the mid century and the end of the century. The development of affected foehn pixels until 2100 is visible for the MPI rcp85 model in fig. 4.17. The development for other models are again visible in appendix A.4 and A.5. Over the years general foehn occurrence is decreasing while widespread events tend to increase, indicated by higher occurrences in the Alps' outliers further away from the main ridge towards the end of the century. The opposite trend is visible in Osttirol confirming the results in fig. 4.14.

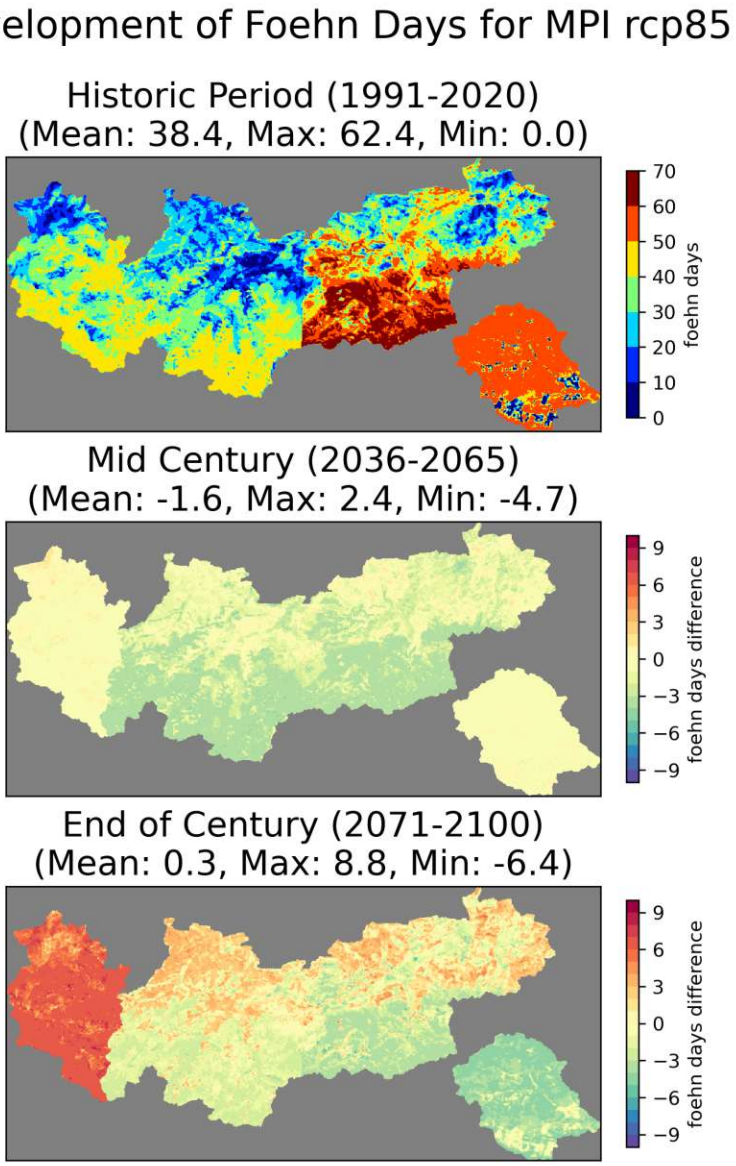

Figure 4.17.: *MPI rcp85 temporal evolution of pixels affected by foehn. The top plot shows the absolute average values of foehn days per year at a pixel in the historic period (1991-2020), while the middle one shows the difference to the absolute numbers in the mid century (2036-2065) and the bottom one the difference towards the end of the century (2071-2100). Mean, maximum and minimum values are calculated over the whole area.*

5. Conclusion and Outlook

By applying OFC a foehn training data set for four regions over Western Austria was generated, yielding reasonable foehn occurrence percentages for all the regions. The seasonality of the occurrences is in agreement with expert's judgement. Training of XGBoost algorithms was done with accuracies of over 95 % for every region when classifying between foehn and no foehn. Similar accuracies for classifying between localised and widespread foehn events were achieved, besides Tiroler Unterland, where an accuracy of 84.1 % marked the lowest accuracy. The analysis of feature importance yielded the physically relevant cross-alpine pressure gradient as dominant feature for most cases. The location of the most important features was not within the borders of the regions for the majority of the eight algorithms. The algorithms were able to generalise on different time periods and models independently of station data. By comparing the seasonality of foehn occurrence in the historic period, it was confirmed, that the EURO-CORDEX models were suitable for generating foehn-producing synoptic patterns. Osttirol hereby did not show a pronounced seasonal trend. By applying the XGBoost algorithms to EURO-CORDEX models and the ERA5 reanalysis, foehn occurrence was predicted within a 2.5 % similarity to the training data. North foehn over Osttirol tended to be overestimated the most.

The replacement of ground wind fields during foehn days has successfully produced the desired higher wind speeds on foehn affected slopes and valley elevations, yielding a high-resolution product with wind climatologies directly considering foehn with different intensities and in different locations for Western Austria. The temporal trend in the MPI rcp85 shows a decreasing trend for foehn except for Vorarlberg and a trend to more widespread events in all regions but Osttirol.

As the study area was Western Austria, which is to the north of the Alps' crest, the thesis' work was more focused on improving south foehn than north foehn detection. The missing seasonal trend and higher overestimation of north foehn in Osttirol could be indicators, that south foehn as a pre-frontal phenomenon is better recognisable in synoptic patterns than the post-frontal north foehn in the EURO-CORDEX models and therefore different or more meteorological variables have to be considered for more accurate classification in Osttirol. The study area could also be extended to Carinthia to provide more cases of north foehn to improve classification quality.

To validate and possibly improve the detection of foehn events out of synoptic reanalysis and climate projection data, the XGBoost algorithms could be compared to other machine learning approaches like convolutional neural networks (CNNs) or detection algorithms with human-set hard thresholds for different variables. Furthermore, bias correction could be applied to the EURO-CORDEX models to transform the value range of meteorological variables closer to ERA5.

The XGBoost models created in this thesis will be applied on every suitable model of the OEKS-15 ensemble of EURO-CORDEX climate scenarios [45] to be able to make more confident predictions about how foehn seasonality and intensity will change in the wake of climate change until 2100. By comparing the foehn seasonality of the models with reanalysis data in the historic period and its statistical parameters, it will be assured that all individual EURO-CORDEX models are able to reproduce weather patterns representing foehn. More robust predictions of how foehn frequency and seasonality will change over the course of different RCPs during the 21st century in Western Austria can be given through applying the algorithms on the suitable models of the ensemble. The representativeness for the specific RCPs of the three models used in this thesis could be assessed by comparing them with the whole ensemble.

Furthermore, the foehn training data set can be published to promote open access science and better reproducibility.

Acknowledgements

I want to thank Dr. Herbert Formayer for the exceptional supervision at BOKU. Over the last years he has grown to be a mentor to me, who constantly challenges me to achieve more while never forgetting the humane side of life. His prudence and views on the role of science in society are things I admire.

Further I want to thank Dr. Florian Libisch, who was so kind to supervise me at TU Wien and therefore made my master thesis possible.

I want to thank my colleagues at BOKU, Fabian Lehner MSc, Katherina Perny MSc and Tatiana Klisho MSc. You were so welcoming and make the workspace an interesting, fun and socially soothing environment. I especially want to thank Fabian for his supervision and meaningful contributions. Every institution would profit from having someone like him.

I also want to thank my fellow students and first-semester-friends Florian Gisinger, Felix Wodaczek, Simon Horvath and Tobias Peherstorfer. Thank you for lifting each other up during intense times, suffering together during hour-long math problems and making it out fine. I can't wait to see where our journeys will take us. Also Felix, thank you for proofreading!

Furthermore I want to thank my parents. Thank you for making it possible for me to pursue an university degree although this is a path you never had the chance to walk.

Last but definitely not least I want to thank my partner Lisa. You are my constant in troubling times and support me in becoming a version of me I am very content with. I will always be thankful for your love.

List of Figures

List of Tables

List of Abbreviations

ARW	Advanced Research WRF
BOKU	University of Natural Resources and Life Sciences, Vienna
CMIP	Coupled Model Intercomparison Projects
CNN	Convolutional Neural Network
ECMWF	European Centre for Medium-Range Weather Forecasts
ECMWF-IFS	ECMWF - Integrated Forecasting System
ERA5	ECMWF Reanalysis 5th Generation
GCM	General Circulation Model
ICHEC rcp85	EURO-CORDEX model ICHEC-EC-EARTH_rcp85_r12i1p1_SMHI-RCA4
INCA	Integrated Nowcasting through Comprehensive Analysis
MPI rcp45	EURO-CORDEX model MPI-M-MPI-ESM-LR_rcp45_r1i1p1_CLMcom-CCLM4-8-17
MPI rcp85	EURO-CORDEX model MPI-M-MPI-ESM-LR_rcp85_r1i1p1_CLMcom-CCLM4-8-17
MSLP	Mean Sea Level Pressure
NWP	Numerical Weather Prediction
OFC	Objective Foehn Classification
RCM	Regional Climate Model
RCP	Representative Concentration Pathways
RMSE	Root Mean Square Error
TAWES	Semi-Automatic Weather Stations (from german Teil-Automatisches Wetter Erfassungs-System)
WMO	World Meteorological Organization
WRF	Weather Research and Forecasting Model
ZAMG	Central Institute for Meteorology and Geodynamics

Bibliography

[1] World Meteorological Organization. "International meteorological vocabulary". In: *WMO/OMM/BMO No. 182* (1992).

[2] S Drechsel and G J Mayr. "Objective Forecasting of Foehn Winds for a Subgrid-Scale Alpine Valley". In: *Weather and Forecasting* 23.2 (Apr. 2008), pp. 205–218. DOI: 10.1175/2007waf2006021.1.

[3] C D Whiteman. *Mountain Meteorology: Fundamentals and Applications*. Oxford University Press, Aug. 2000. ISBN: 9780195132717. DOI: 10.1093/oso/9780195132717.001.0001.

[4] L Sfîcă et al. "Cotnari Vineyard - a gift of hydraulic foehn?" In: *Lucrări Ştiinţifice. Seria Agronomie* 57 (Dec. 2014), pp. 227–332.

[5] D Plavcan, G J Mayr, and A Zeileis. "Automatic and Probabilistic Foehn Diagnosis with a Statistical Mixture Model". In: *Journal of Applied Meteorology and Climatology* 53.3 (Mar. 2014), pp. 652–659. DOI: 10.1175/jamc-d-13-0267.1.

[6] Zentralanstalt für Meteorologie und Geodynamik (ZAMG). *INCA*. https://www.zamg.ac.at/cms/de/forschung/wetter/inca. accessed: 2023-01-04. 2020.

[7] T Haiden et al. "The Integrated Nowcasting through Comprehensive Analysis (INCA) System and Its Validation over the Eastern Alpine Region". In: *Weather and Forecasting* 26.2 (Apr. 2011), pp. 166–183. DOI: 10.1175/2010waf2222451.1.

[8] F Lehner et al. *Klimatologische Daten für die Klimawandelanpassung der Tiroler und Vorarlberger Wälder durch Kombination mit dynamischen Klimaszenarien (BIOCLIM)*. German. Tech. rep. Institute of Meteorology, Climatology (BOKU-Met), University of Natural Resources, and Life Sciences, Vienna, 2023.

[9] W C Skamarock et al. "A Description of the Advanced Research WRF Model Version 4.3". In: (2021). DOI: 10.5065/1DFH-6P97.

[10] R G Barry. *Mountain Weather and Climate*. 3rd edition. Cambridge University Press, 2008. DOI: 10.1017/cbo9780511754753.

[11] P Seibert. "Hann's Thermodynamic Foehn Theory and its Presentation in Meteorological Textbooks in the Course of Time". In: 2004.

[12] J Hann. "Some remarks about the development of views on the origin of the foehn (orig. german: Einige Bemerkungen zur Entwickelungs-Geschichte der Ansichten über den Ursprung des Foehn)". In: *Meteorologische Zeitschrift* 21.6 (Dec. 2012), pp. 591–596. DOI: 10.1127/0941-2948/2012/0533.

[13] M Kuhn. *Föhnstudien*. German. Wissenschaftliche Buchgesellschaft, 1989. ISBN: 9783534091553.

[14] B Klose. *Meteorologie - Eine interdisziplinäre Einführung in die Physik der Atmosphäre*. German. 1st edition. Springer Berlin Heidelberg, 2016. DOI: 10.1007/978-3-662-43622-6.

[15] H Richner and P Hächler. "Understanding and forecasting Alpine foehn". In: *Mountain Weather Research and Forecasting: Recent Progress and Current Challenges*. Springer Netherlands, Apr. 2012, pp. 219–260. DOI: 10.1007/978-94-007-4098-3_4.

[16] P Seibert. "South foehn studies since the ALPEX experiment". In: *Meteorology and Atmospheric Physics* 43.1-4 (1990), pp. 91–103. DOI: 10.1007/bf01028112.

[17] R Steinacker. "Alpiner Föhn – eine neue Strophe zu einem alten Lied". German. In: *promet, Jahrgang.32*. Vol. 1/2. Deutscher Wetterdienst, Mar. 2006, pp. 3–10.

[18] J Vergeiner. "South foehn studies and a new foehn classification scheme in the Wipp and Inn Valley". PhD thesis. Department of Meteorology and Geophysics, University of Innsbruck, Nov. 2004.

[19] F Föst. "Eine objektive Föhnklimatologie für das Wipp- und Inntal". German. MA thesis. Facbereich Geowissenschaften,Freie Universität Berlin, Feb. 2006.

[20] A Gohm and G J Mayr. "Hydraulic aspects of fo¨hn winds in an Alpine valley". In: *Quarterly Journal of the Royal Meteorological Society* 130.597 (Jan. 2004), pp. 449–480. DOI: 10.1256/qj.03.28.

[21] A Gohm and G J Mayr. "Schnelle Strömungen durch Gebirgseinschnitte". German. In: *promet, Jahrgang.32*. Vol. 1/2. Deutscher Wetterdienst, Mar. 2006, pp. 11–17.

[22] European Centre for Medium-Range Weather Forecasts (ECMWF). *ERA5: data documentation*. https://confluence.ecmwf.int/display/CKB/ERA5%3A+data+documentation. accessed: 2023-02-07. 2020.

[23] H Formayer. "personal conversation". Feb. 2023.

[24] C Cetti, B Buzzi, and M Sprenger. "Climatology of Alpine north foehn". In: *Scientific Report MeteoSwiss* 100 (2015).

[25] D Bolton. "The Computation of Equivalent Potential Temperature". In: *Monthly Weather Review* 108.7 (July 1980), pp. 1046–1053. DOI: 10.1175/1520-0493(1980)108<1046:tcoept>2.0.co;2.

[26] B Dürr. "Automatisiertes Verfahren zur Bestimmung von Föhn in Alpentälern". German. In: *Arbeitsberichte der MeteoSchweiz* 223 (2008).

[27] C Mony, L Jansing, and M Sprenger. "Evaluating foehn occurrence in a changing climate based on reanalysis and climate model data using machine learning". In: *Weather and Forecasting* 36 (Dec. 2021), pp. 2039–2055. DOI: 10.1175/waf-d-21-0036.1.

[28] M Sprenger et al. "Nowcasting Foehn Wind Events Using the AdaBoost Machine Learning Algorithm". In: *Weather and Forecasting* 32.3 (May 2017), pp. 1079–1099. DOI: 10.1175/waf-d-16-0208.1.

[29] D S Morgenstern. "Multidecadal Foehn time series reconstruction using machine learning and ERA5 reanalysis data". MA thesis. Faculty of Geo- and Atmospheric Sciences, University of Innsbruck, Jan. 2020.

[30] T Chen and C Guestrin. "XGBoost: A Scalable Tree Boosting System". In: *Proceedings of the 22nd ACM SIGKDD International Conference on Knowledge Discovery and Data Mining*. ACM, Aug. 2016, pp. 785–794. DOI: 10.1145/2939672.2939785.

[31] L Breiman. "Random Forests". In: *Machine Learning* 45.1 (2001), pp. 5–32. DOI: 10.1023/a:1010933404324.

[32] S S Azmi and S Baliga. "An overview of boosting decision tree algorithms utilizing AdaBoost and XGBoost boosting strategies". In: *International Research Journal of Engineering and Technology (IRJET)* 7.5 (May 2020), pp. 6867–6870.

[33] K Janocha and W M Czarnecki. *On Loss Functions for Deep Neural Networks in Classification*. Feb. 2017. DOI: 10.48550/ARXIV.1702.05659.

[34] W Roedel and T Wagner. *Physik unserer Umwelt: Die Atmosphäre*. German. 5th edition. Springer Berlin Heidelberg, 2017. DOI: 10.1007/978-3-662-54258-3.

[35] The Intergovernmental Panel on Climate Change (IPCC). *The Physical Science Basis. Contribution of Working Group I to the Fourth Assessment Report of the Intergovernmental Panel on Climate Change*. 2007.

[36] R McSweeny and Z Hausfather. *Q&A: How do climate models work?* https://www.carbonbrief.org/qa-how-do-climate-models-work/. accessed: 2023-02-05. Jan. 2018.

[37] D P van Vuuren et al. "The representative concentration pathways: an overview". In: *Climatic Change* 109.1-2 (Aug. 2011), pp. 5–31. DOI: 10.1007/s10584-011-0148-z.

[38] K E Taylor, R J Stouffer, and G A Meehl. "An Overview of CMIP5 and the Experiment Design". In: *Bulletin of the American Meteorological Society* 93.4 (Apr. 2012), pp. 485–498. DOI: 10.1175/bams-d-11-00094.1.

[39] National Oceanic and Atmospheric Administration (NOAA). *The First Climate Model*. https://celebrating200years.noaa.gov/breakthroughs/climate_model/welcome.html#model. accessed: 2023-02-05. 2022.

[40] D Maraun and M Widmann. *Statistical Downscaling and Bias Correction for Climate Research*. Cambridge University Press, Dec. 2017. ISBN: 9781107588783. DOI: 10.1017/9781107588783.

[41] V Djurdjevic and B Rajkovic. "Development of the EBU-POM coupled regional climate model and results from climate change experiments". In: *Advances in Environmental Modelling and Measurements*. Nova Publishers, 2010.

[42] Copernicus Climate Change Service (C3S). *ERA5: Fifth generation of ECMWF atmospheric reanalyses of the global climate*. Copernicus Climate Change Service Climate Data Store (CDS), https://cds.climate.copernicus.eu/cdsapp#!/home. accessed: 2022-12-21. 2017.

[43] H Hersbach et al. "The ERA5 global reanalysis". In: *Quarterly Journal of the Royal Meteorological Society* 146.730 (June 2020), pp. 1999–2049. DOI: 10.1002/qj.3803.

[44] D Jacob et al. "EURO-CORDEX: new high-resolution climate change projections for European impact research". In: *Regional Environmental Change* 14.2 (July 2013), pp. 563–578. DOI: 10.1007/s10113-013-0499-2.

[45] Federal Ministry of the Republic of Austria for Climate Action, Environment, Energy, Mobility, Innovation and Technology. *Endbericht OEKS15| Klimaszenarien für Österreich | Daten - Methoden - Klimaanalyse*. German. https://www.bmk.gv.at/themen/klima_umwelt/klimaschutz/anpassungsstrategie/publikationen/oeks15.html. accessed: 2023-01-04. 2015.

[46] Zentralanstalt für Meteorologie und Geodynamik (ZAMG). *TAWES stations: semi-automatic weather stations*. https://www.zamg.ac.at/cms/en/climate/meteorological-network. accessed: 2023-01-04.

[47] C Saunders, A Gammermann, and V Vovk. "Ridge Regression Learning Algorithm in Dual Variables". In: *15th International Conference on Machine Learning 1998 (ICML '98)*. 1998, pp. 515–521.

[48] A J Cannon, S R Sobie, and T Q Murdock. "Bias Correction of GCM Precipitation by Quantile Mapping: How Well Do Methods Preserve Changes in Quantiles and Extremes?" In: *Journal of Climate* 28.17 (Sept. 2015), pp. 6938–6959. DOI: 10.1175/jcli-d-14-00754.1.

[49] K Pearson. "VII. Note on regression and inheritance in the case of two parents". In: *Proceedings of the Royal Society of London* 58.347-352 (Dec. 1895), pp. 240–242. DOI: 10.1098/rspl.1895.0041.

[50] M Rotach. *personal communication*. Oct. 2022.

A. Appendix

A.1. Selected Fingerprints

Table A.1.: *Selected WRF simulated dates for physically possible fingerprints. The columns describe, which intensity foehn has in the stated region. A fingerprint was considered as physical possible if adjacent regions had a foehn intensity, which was differing by only one level where levels are no, localised or widespread foehn.*

Date	Vorarlberg	Tiroler Oberland	Tiroler Unterland	Osttirol
2017-03-03 14:40	Localised	Localised	Localised	No
2017-02-27 17:00	Localised	Localised	Widespread	No
2017-03-03 09:00	Localised	No	Localised	No
2017-03-03 07:00	Localised	No	No	No
2017-12-11 11:00	Localised	Widespread	Localised	No
2017-12-11 11:00	Localised	Widespread	Widespread	No
2017-02-28 10:30	No	Localised	Localised	No
2017-12-12 10:20	No	Localised	No	No
2016-09-15 10:10	No	Localised	Widespread	No
2016-09-15 12:00	No	No	Localised	No
2020-10-03 10:00	No	No	Widespread	No
2017-12-11 19:30	No	Widespread	Widespread	No
2017-03-04 01:00	Widespread	Localised	Localised	No
2017-03-04 01:00	Widespread	Localised	No	No
2017-03-04 06:30	Widespread	Localised	Widespread	No
2017-03-04 12:00	Widespread	Widespread	Localised	No
2017-12-11 11:00	Widespread	Widespread	Widespread	No
2018-11-27 12:20	No	No	No	Localised
2017-10-30 00:30	No	No	No	Widespread

Table A.2.: *Selected substitution dates for detected physically impossible occurrences. The columns describe, which intensity foehn has in the stated region, yielding physically impossible behaviour. Still only pixels in the regions, which were detected, where treated as foehn pixels when they exceeded the windspeed limit.*

Date	Vorarlberg	Tiroler Oberland	Tiroler Unterland	Osttirol
2017-12-11 11:00	No	Widespread	No	No
2017-12-11 11:00	No	Widespread	Localised	No
2017-12-11 11:00	Localised	Widespread	No	No
2017-03-04 01:00	Widespread	No	No	Localised
2017-03-04 01:00	Widespread	No	Localised	No
2017-03-04 01:00	Widespread	No	No	No
2017-03-03 14:40	Localised	Localised	Localised	Localised
2017-03-03 14:40	Localised	Localised	No	No
2017-02-27 17:00	Localised	No	Widespread	No
2017-03-04 06:30	Widespread	No	Widespread	No
2016-09-15 10:10	No	No	Widespread	No
2017-03-03 07:00	Localised	No	No	Localised
2017-10-30 00:30	Localised	No	No	Widespread
2017-02-28 10:30	No	Localised	Localised	Localised
2017-12-12 10:20	No	Localised	No	Localised
2017-03-04 12:00	Widespread	Widespread	No	No

A.2. XGBoost Hyperparameter Selection

Table A.3.: *XGBoost hyperparameter selection. After using a grid search with a cross-validation of five random sets from the feature matrix for each of the eight algorithms visible in the first column, parameter values visible in the other columns yielded the best average accuracy of the cross-validation. Loc and wide are short forms of localised and widespread.*

Algorithm	eval metric	gamma	learning rate	max depth	min child weight	objective	reg lambda
Vorarlberg yes/no	error	1.5	0.3	9	10	binary:logitraw	2.5
Vorarlberg loc/wide	logloss	1	0.8	7	1	binary:logitraw	2.5
Tiroler Oberland yes/no	error	1.5	0.3	9	10	binary:logitraw	2.5
Tiroler Oberland loc/wide	logloss	1	0.8	7	1	binary:logitraw	2.5
Tiroler Unterland yes/no	error	1	0.3	9	5	binary:logitraw	1.5
Tiroler Unterland loc/wide	error	1	0.5	5	10	binary:logitraw	2.5
Osttirol yes/no	error	1.5	0.1	9	5	binary:logitraw	1.0
Osttirol loc/wide	error	2	0.3	9	1	binary:logitraw	0.3

A.3. North Foehn Climatologies

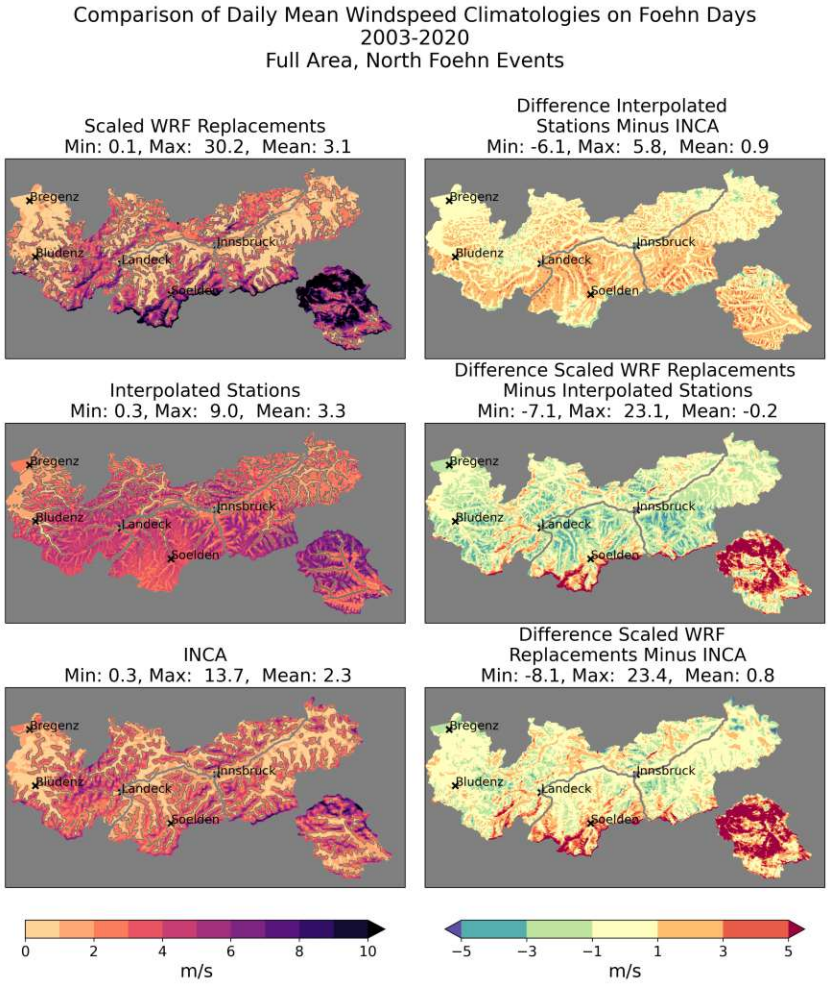

Figure A.1.: *Spatial comparison of climatologies of north foehn days within the INCA period (2003-2020). The first column shows absolute values of wind speed climatologies in* m/s *while the second shows the difference of the individual climatologies in* m/s*. The thin grey lines in the first column show, where the wind speed condition for counting as foehn affected is satisfied. Several locations are displayed with black crosses and their name for better orientation. The rivers Inn and Sill are drawn in grey lines. Mean, maximum and minimum values are calculated over the whole area. Wind speeds in Osttirol are significantly higher and smaller in other upper elevations. The total spatial mean of the differences is close to 0, with* $-0.2\,\mathrm{m/s}$ *compared to the wind field generated from interpolating stations and* $0.8\,\mathrm{m/s}$ *compared to INCA.*

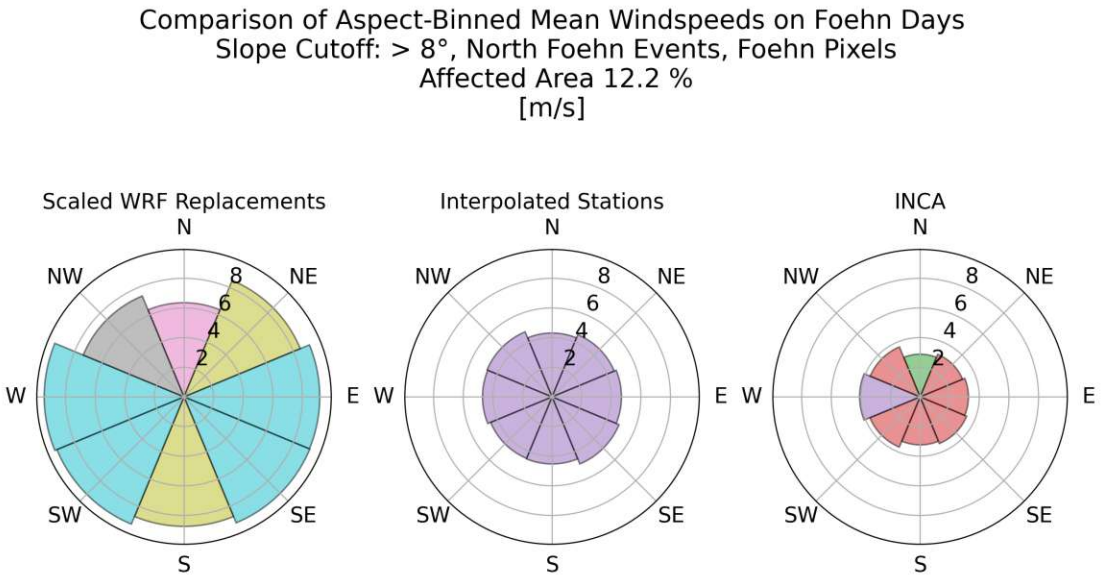

Figure A.2.: *Wind speed climatologies at affected pixels during north foehn days, aspect binned wind roses in* m/s. *The compass directions describe where the aspect of the slopes point. One aspect covers a range of* 45°. *Matching colours are used for matching integer ranges. A total area of 12.2 % is affected by north foehn when considering slopes with inclination above* 8°. *Osttirol is a small region compared to the total area. Wind speeds are significantly higher in the south directed slopes here.*

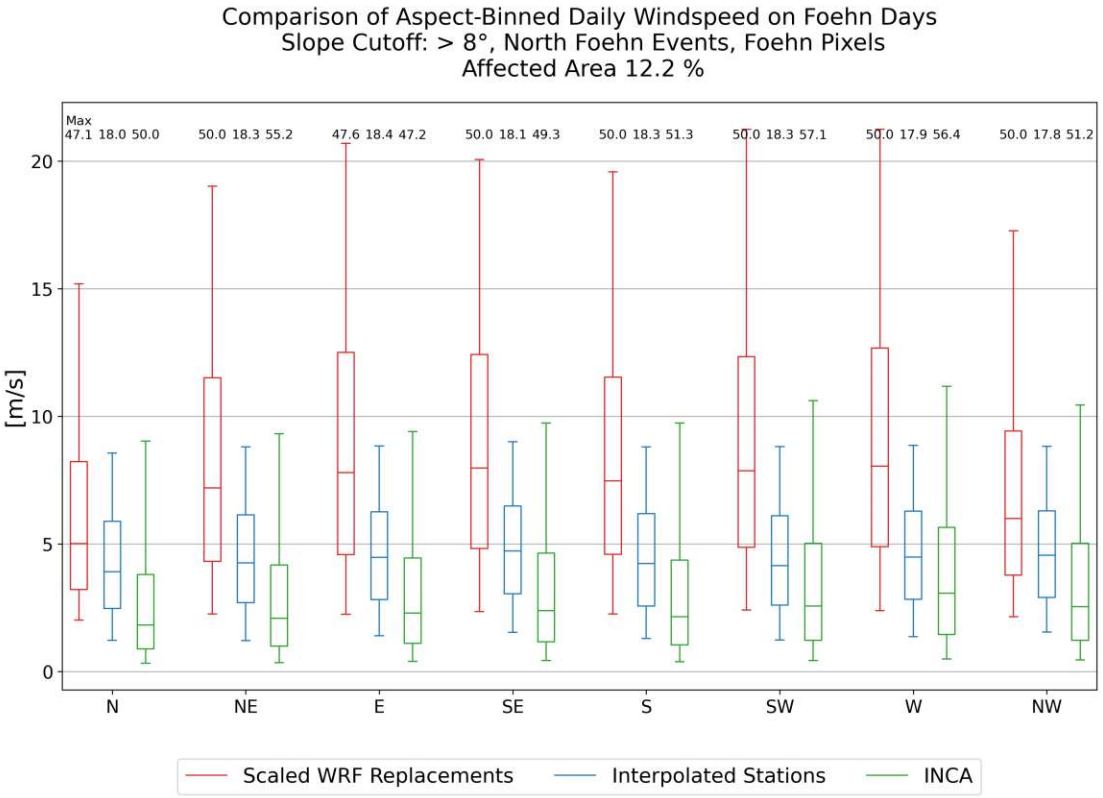

Figure A.3.: *Wind speed climatologies at affected pixels during north foehn days, aspect binned boxplots. The compass directions on the horizontal axis describe where the aspect of the slopes point. One aspect covers a range of* 45°. *The vertical axis describes wind speeds in* m/s. *The whiskers cover the* 5^{th} *and* 95^{th} *percentile. The maxima are displayed as numbers above. A total area of 12.2 % is affected by north foehn when considering slopes with inclination above* 8°. *Higher wind speeds in Osttirol are observed on slopes perpendicular to the Alpine ridge.*

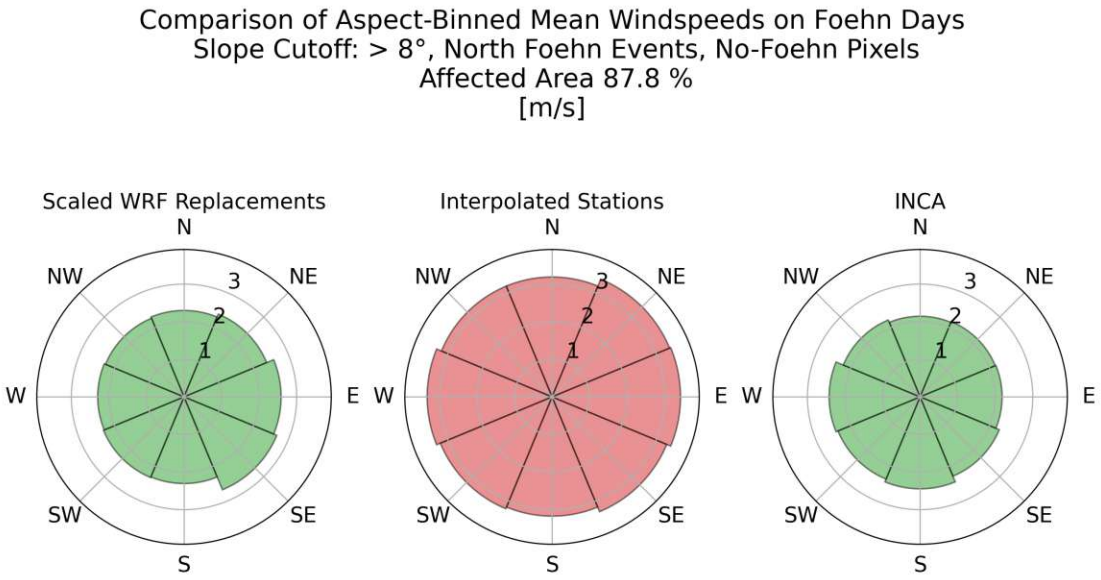

Figure A.4.: *Wind speed climatologies at foehn free pixels during north foehn, aspect binned wind roses in* m/s. *The compass directions describe where the aspect of the slopes point. One aspect covers a range of* 45°. *Matching colours are used for matching integer ranges. A total area of 87.8 % is not affected by north foehn when considering slopes with inclination above* 8°. *The range of wind speed values of the scaled WRF replacements over the unaffected pixels, which are Vorarlberg, Tiroler Oberland and Tiroler Unterland for the most part, are in a similar range of INCA. The wind field generated of interpolated station data yields higher values. No clear direction trend is visible.*

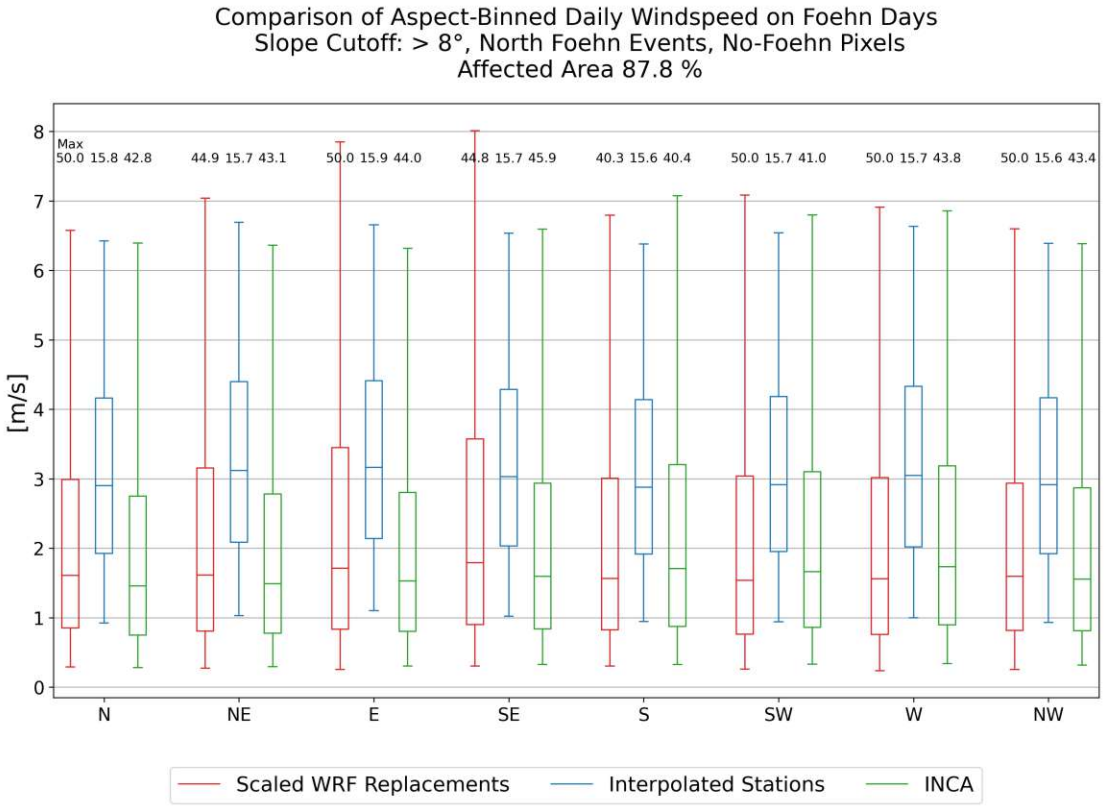

Figure A.5.: *Wind speed climatologies at foehn free pixels during north foehn, aspect binned boxplots. The compass directions on the horizontal axis describe where the aspect of the slopes point. One aspect covers a range of* 45°. *The vertical axis describes wind speeds in* m/s. *The whiskers cover the* 5^{th} *and* 95^{th} *percentile. The maxima are displayed as numbers above. A total area of 87.8 % is not affected by north foehn when considering slopes with inclination above* 8°. *The spread of the scaled WRF replacements is larger while the medians are close to the ones of INCA.*

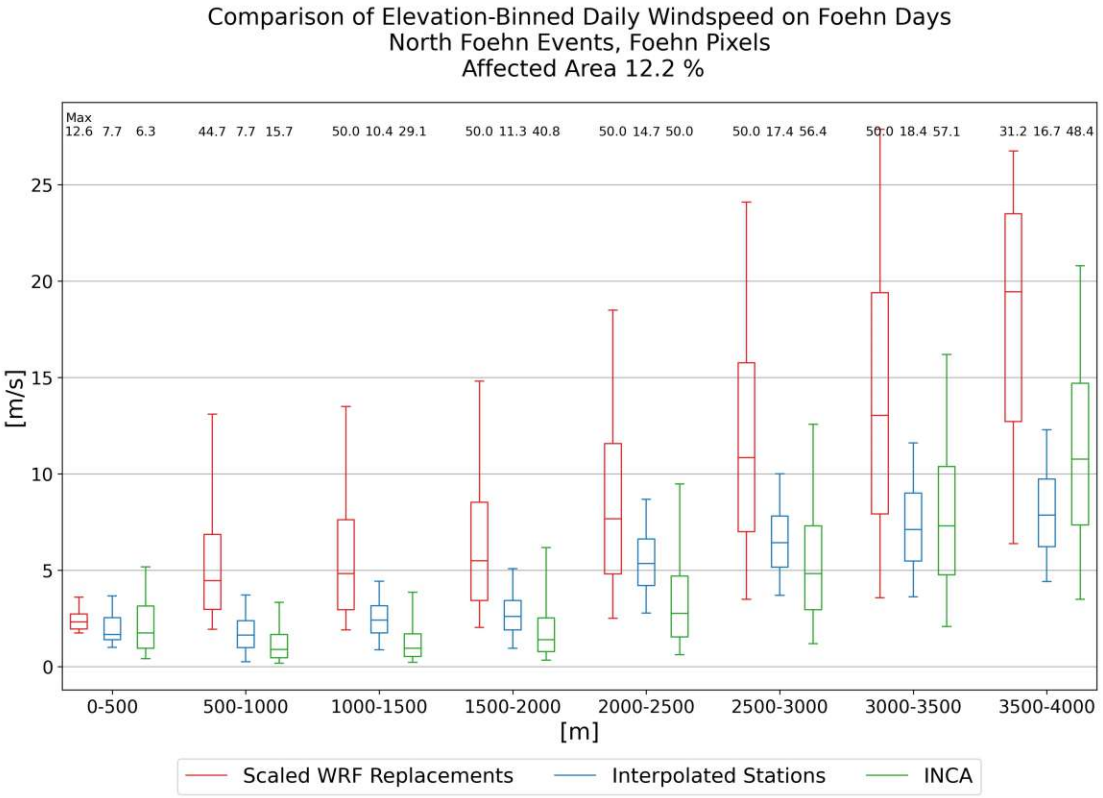

Figure A.6.: *Wind speed climatologies at foehn affected pixels during north foehn days, elevation binned boxplots. The horizontal axis describes elevation bins in* m. *The vertical axis describes wind speeds in* m/s. *The whiskers cover the* 5^{th} *and* 95^{th} *percentile. The maxima are displayed as numbers above. A total area of 12.2 % is affected by north foehn when considering slopes with inclination above* 8°. *A high elevation dependency is visible in the scaled WRF replacements. Wind speeds in the valley regions, which are in the 500 - 1000 m class, are significantly higher than in the other wind fields.*

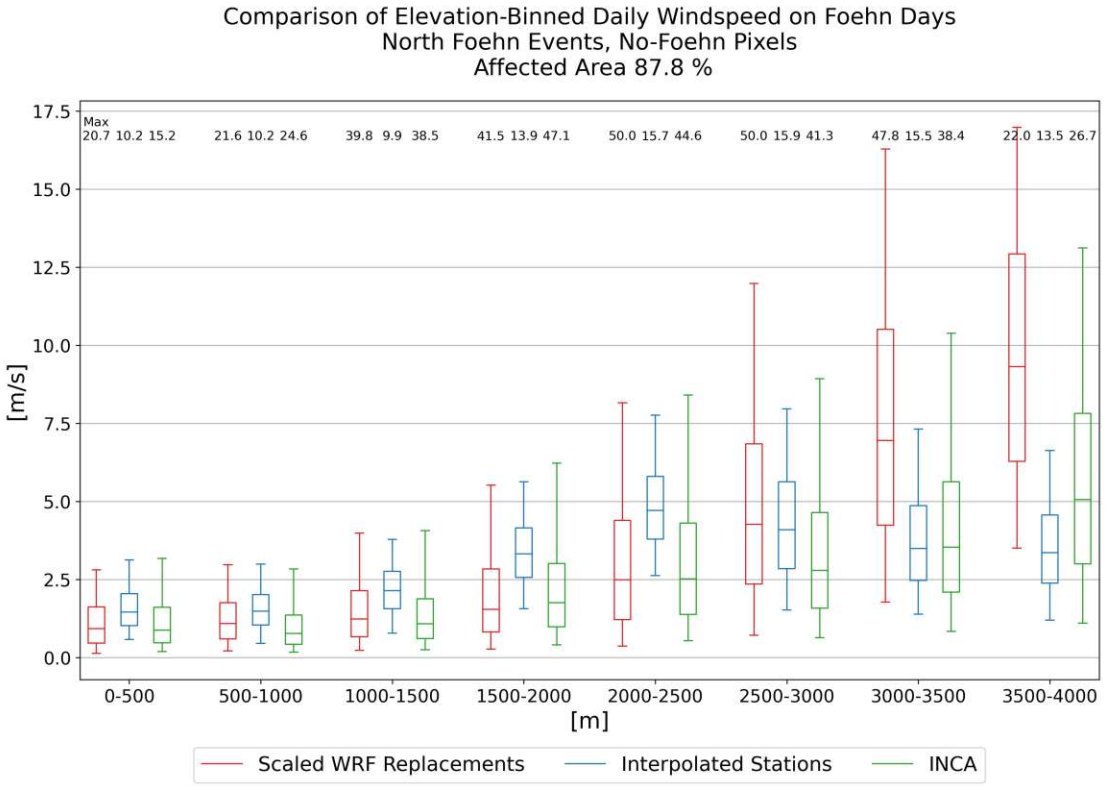

Figure A.7.: *Wind speed climatologies at foehn free pixels during north foehn, elevation binned boxplots. The horizontal axis describes elevation bins in* m. *The vertical axis describes wind speeds in* m/s. *The whiskers cover the* 5^{th} *and* 95^{th} *percentile. The maxima are displayed as numbers above. A total area of 87.8 % is not affected by north foehn when considering slopes with inclination above* 8°. *A strong elevation dependency is observed in all three wind fields. For foehn free pixels the elevation dependency is more in sync with each other and wind speeds in the valley elevations are lower.*

A.4. Temporal Trends of Model MPI rcp45

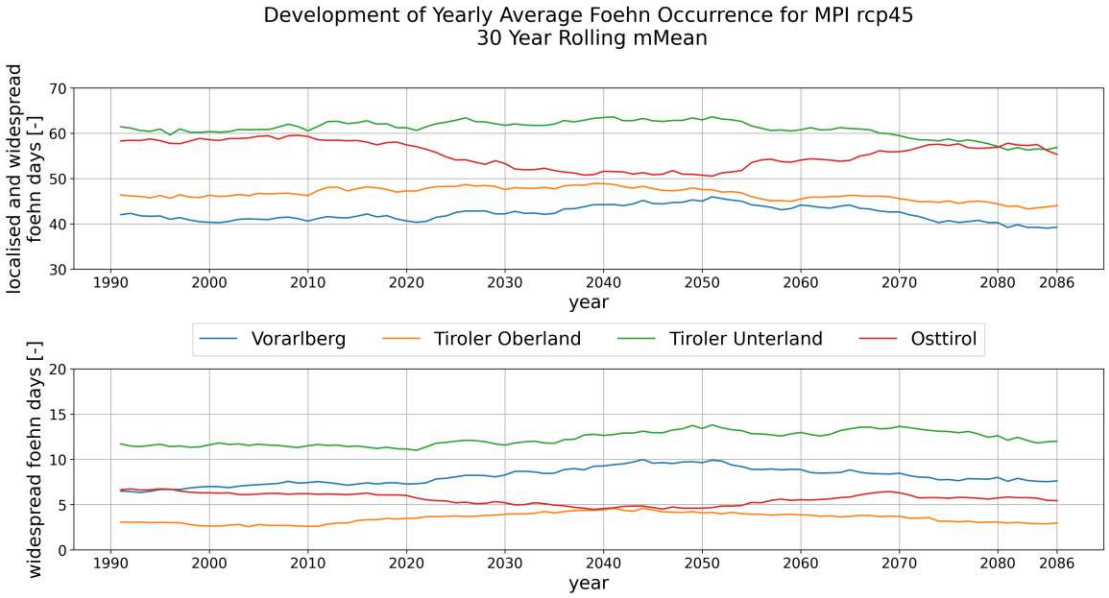

Figure A.8.: *MPI rcp45 foehn development until 2086. The horizontal axis describes the years, while the vertical axis states average foehn days per year. The regions are colour-coded and visible in the legend. A rolling mean of 30 years is applied to smooth the curve. Because of that the last available year is 2086 as the climate models reach until 2100. With RCP 4.5, the less fossil fuel intensive pathway, weak trends are observable, with the strongest positive (negative) deviations in the mid of the century for south (north) foehn.*

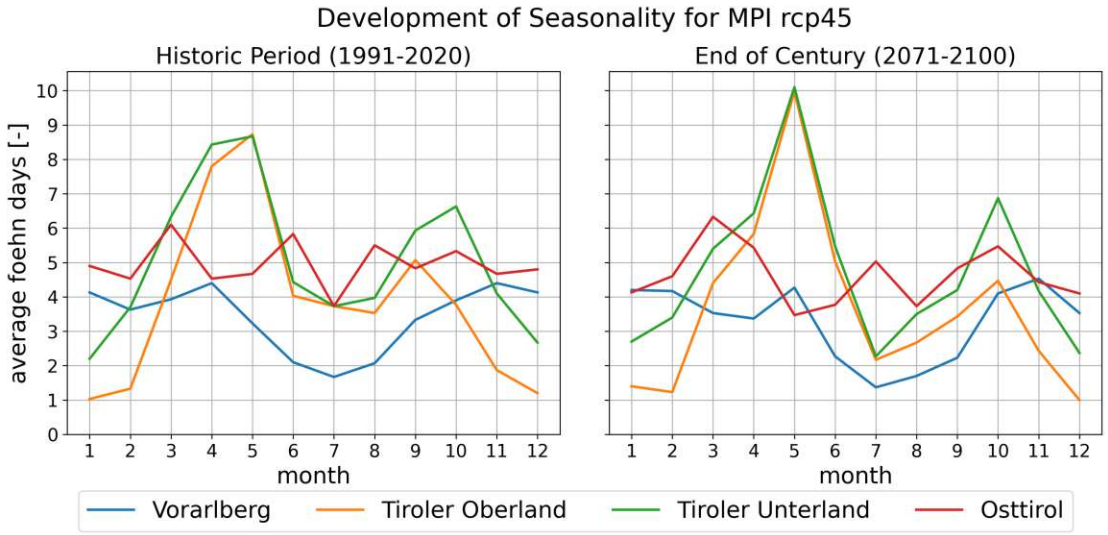

Figure A.9.: *MPI rcp45 foehn seasonality development until 2100. Compared are the historic period (1991-2020) and the end of the century (2071-2100) of the specific model. Regions are colour-coded and visible in the legend. The horizontal axis describes the months of the year, the vertical axis the accumulated average foehn days on monthly basis. Most months tend to have less foehn towards the end of the century, while May is showing the opposite trend.*

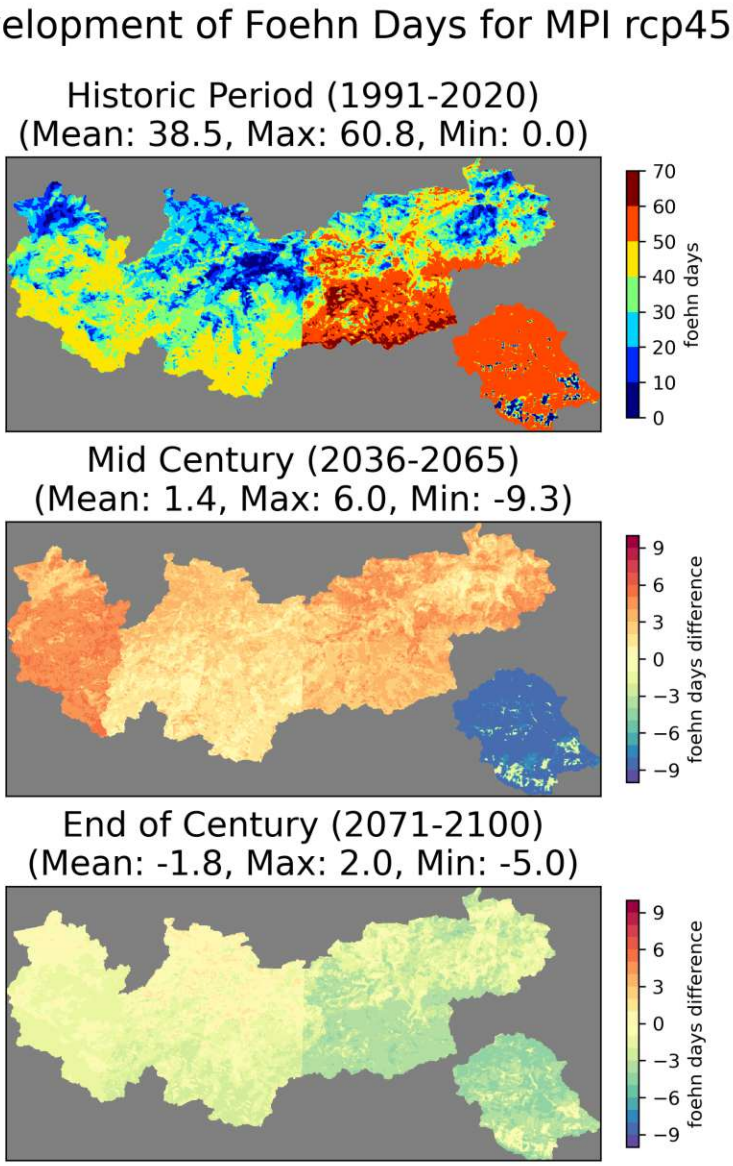

Figure A.10.: *MPI rcp45 temporal evolution of pixels affected by foehn. The top plot shows the absolute average values of foehn days per year at a pixel in the historic period (1991-2020), while the middle one shows the difference to the absolute numbers in the mid century (2036-2065) and the bottom one the difference towards the end of the century (2071-2100). Mean, maximum and minimum values are calculated over the whole area. A positive trend for the mid century can be seen for south foehn, while north foehn has the a negative trend. By the end of the century, a negative trend is visible for all regions.*

A.5. Temporal Trends of Model ICHEC rcp85

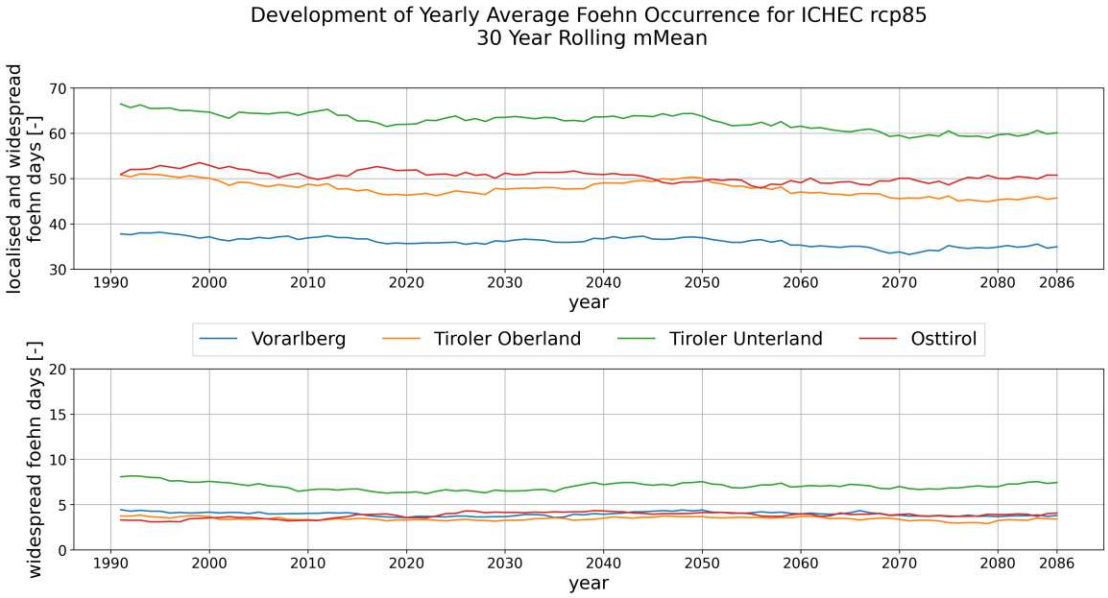

Figure A.11.: *ICHEC rcp85 foehn development until 2086. The horizontal axis describes the years, while the vertical axis states average foehn days per year. The regions are colour-coded and visible in the legend. A rolling mean of 30 years is applied to smooth the curve. Because of that the last available year is 2086 as the climate models reach until 2100. A slight negative trend is visible for all south foehn regions while Osttirol has no trend. No trend for widespread foehn can be detected.*

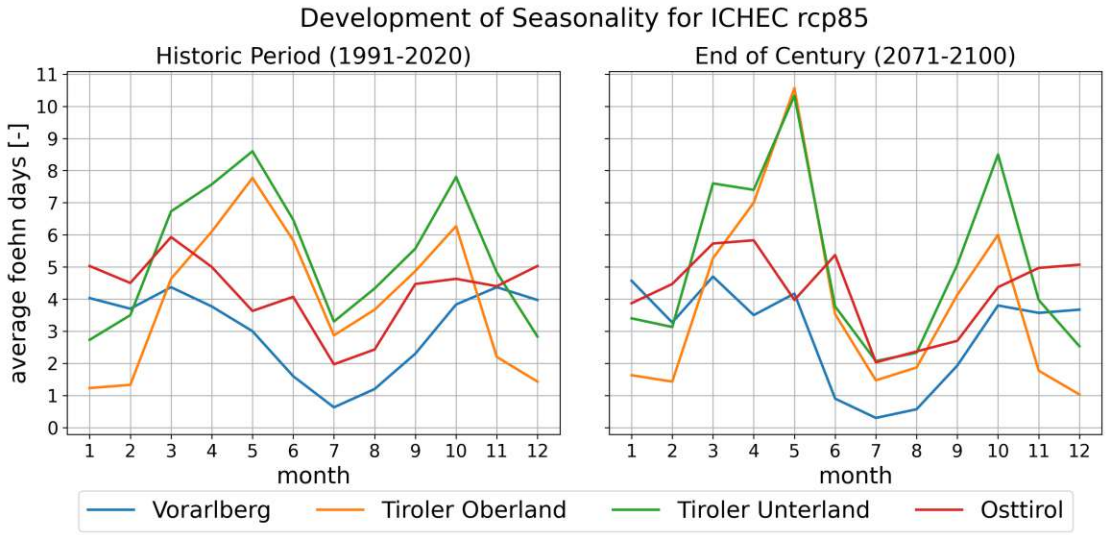

Figure A.12.: *ICHEC rcp85 foehn seasonality development until 2100. Compared are the historic period (1991-2020) and the end of the century (2071-2100) of the specific model. Regions are colour-coded and visible in the legend. The horizontal axis describes the months of the year, the vertical axis the accumulated average foehn days on monthly basis. Summer months in this model tend to have less foehn by the end of the century while spring months tend to have more, especially May.*

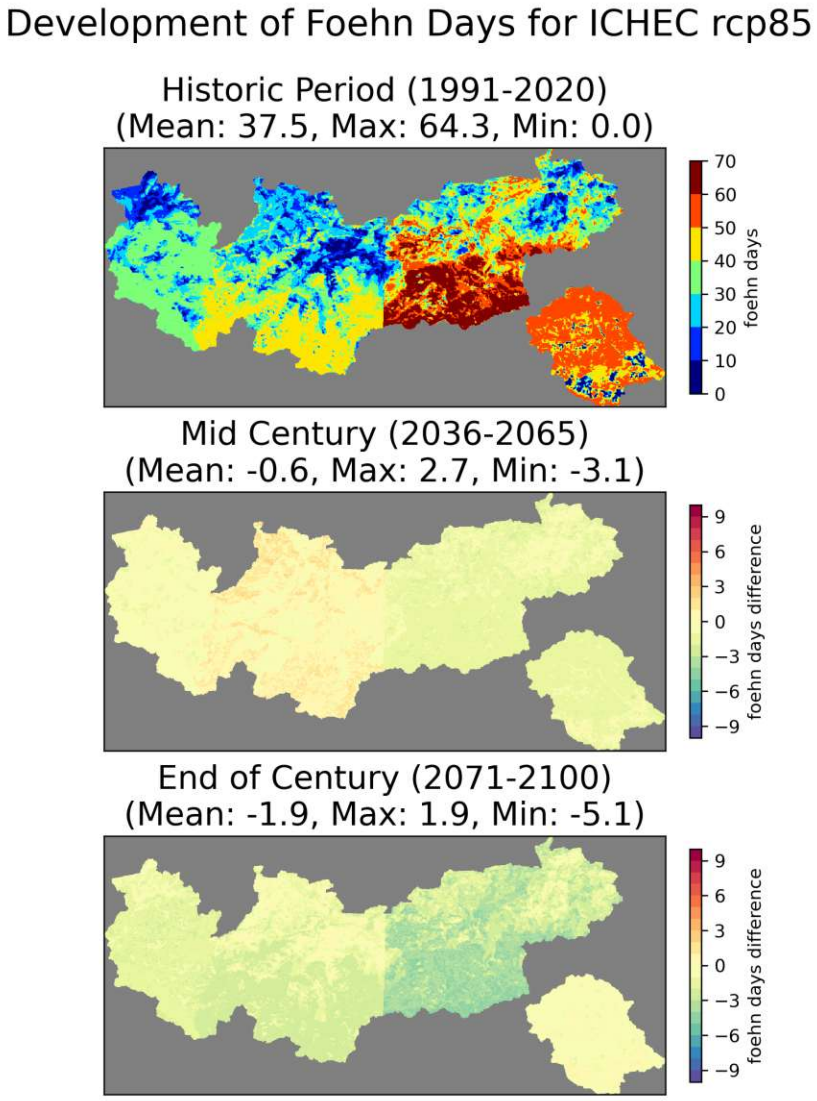

Figure A.13.: *ICHEC rcp85 temporal evolution of pixels affected by foehn. The top plot shows the absolute average values of foehn days per year at a pixel in the historic period (1991-2020), while the middle one shows the difference to the absolute numbers in the mid century (2036-2065) and the bottom one the difference towards the end of the century (2071-2100). Mean, maximum and minimum values are calculated over the whole area. A slight negative trend towards the end of the century is visible for all regions.*